Aristotle University of Thessaloniki
School of Geology
Department of Geophysics

ALMPANIS ANGELOS
GEOLOGIST

CROSS-HOLE ELECTRICAL RESISTIVITY TOMOGRAPHY: APPLICATION OF DIFFERENT ELECTRODE CONFIGURATIONS WITHIN BOREHOLES

“MASTER THESIS”

Postgraduate Program: "Applied and Environmental Geology"

Field of specialization: "Applied Geophysics"

Thessaloniki
October 2018

ALMPANIS ANGELOS

GEOLOGIST

Cross-hole electrical resistivity tomography: Application of different electrode configurations within boreholes.

Submitted to the School of Geology of Aristotle University of Thessaloniki within the postgraduate program Applied and Environmental Geology, with specialization to Applied Geophysics.

Date of Oral Examination: 05/10/2018

Advisory Committee

Professor Panagiotis Tsourlos (Supervisor)

Professor Costas Papazachos (Advisory Committee member)

Associate Professor George Vargemezis (Advisory Committee member)

CROSS-HOLE ELECTRICAL RESISTIVITY TOMOGRAPHY: APPLICATION OF DIFFERENT ELECTRODE CONFIGURATIONS WITHIN BOREHOLES- *Master Thesis*

Acknowledgements

First and foremost, I would like to express my gratitude to my supervisor professor Panagiotis Tsourlos for his constant and valuable guidance throughout my academic years. The assistance and the full support that he has shown is something for which I can only be thankful.

I would also like to express my gratitude to the second advisory committee member and my professor Konstantinos Papazachos for providing me with all the knowledge and inspiration, throughout the postgraduate program.

I am particularly thankful to third advisory committee member and also my professor, George Vargemezis, for his guidance and support over the last 2 years. He gave me the opportunity to participate in several geophysical projects, transferring his knowledge and experience to me.

I couldn’t forget my professor Grigorios Tsokas for teaching me the lessons I needed to learn about my career, showing trust in me and giving me the opportunity to participate in many field surveys.

I acknowledge Dr. Ilias Fikos and Dr. Alexandros Stampolidis. Working with them was very educational and supportive to me.

The field measurements for this study could not be realized without the contribution of my postgraduate classmates, Nikolaos Kordatos, Eftychia Amanatidou, Christos Christoforou, Myrto Groumpa and George Fillipakos. I am thankful to them not only for their help but also for their friendship throughout the last two years.

Last but not least, I would like to thank all the people in my life that have always believed in me and inspired me to complete one more important phase in my life. Especially, I am extremely grateful to my parents for their constant support and encouragement throughout my studies.

Abstract

The subject of this thesis is the study of the applicability of cross borehole electrical resistivity tomography method within plastic cased slotted boreholes. The study involves both experimental and field data trials.

Experimental tests involved performing cross-hole ERT measurements in a tank environment using model plastic PVC cased slotted boreholes, of different slot density, using different electrode configurations, aiming to relate the applicability of this measurement set-up with the density of the borehole slots. An algorithm, coded in Matrix Laboratory (MATLAB) language, was developed for the generation of measuring ERT protocols using different arrays.

Extensive experimental data tests suggested that all arrays could be measured successfully when the horizontal slot density of the plastic boreholes is relatively high (i.e. larger than 5 slots/ electrode spacing). However, as slot density is decreasing inversion results produced from arrays, which were using current and potential electrodes in the same hole (i.e. pole-tripole, bipole-bipole arrays), suffered from severe artefacts. In such a case, only the pole-dipole array can be used successfully.

The above findings were tested in the case of actual field data. Cross-hole ERT data were collected between plastic cased monitoring boreholes placed along the Thessaloniki metro line, which is under construction. Additional measuring strategies between boreholes were also proposed to overcome the limitation of the analysis of the geoelectrical imaging of the subsurface, due to the long distance between the boreholes, either involving ERT surface measurements to the cross-hole ERT data or applying the borehole-to-surface ERT arrangement.

Some of the plastic cased boreholes had an unknown (but of low density) number of slots while some newly constructed ones were build having a high slot density. The produced inversion results verified fully the experimental findings: in low slot density boreholes only the electrode arrays using separate current and potential borehole electrodes produced valid results while all arrays seemed to produce good data in the case of high slot density.

The experimental and field results of this study showed that cross-hole ERT measurements in slotted PVC cased observation wells is feasible. The applicability depends on the density of the slots as in general the denser the slot the better the data quality. Among tested configurations the pole-dipole array (i.e. current electrode not in the same borehole with the potential electrodes) is by far the most preferable array. The above provides a new perspective into the geoelectrical prospecting as it seems that it can be now used in slotted PVC cased observation wells reducing in this way the survey costs and efforts.

Περίληψη

Αντικείμενο της παρούσας διατριβής είναι η μελέτη της εφαρμοσιμότητας της ηλεκτρικής τομογραφίας μέσα σε πλαστικές διάτρητες γεωτρήσεις παρακολούθησης. Η εργασία περιλαμβάνει δεδομένα πειραματικών δοκιμών και δοκιμών πεδίου.

Οι πειραματικές δοκιμές περιλαμβάνουν την πραγματοποίηση μετρήσεων ηλεκτρικής τομογραφίας μεταξύ γεωτρήσεων σε πειραματική δεξαμενή, χρησιμοποιώντας πλαστικά διάτρητα PVC στελέχη γεωτρήσεων, διαφορετικής πυκνότητας σχισμών, χρησιμοποιώντας διαφορετικές διατάξεις ηλεκτροδίων, στοχεύοντας να συσχετίσουμε την εφαρμογή αυτής της διαμόρφωσης μετρήσεων με την πυκνότητα των σχισμών στην γεώτρηση. Ακόμη, αναπτύχθηκε αλγόριθμος, σε γλώσσα Matrix Laboratory (MATLAB), για την παραγωγή πρωτόκολλων μέτρησης ηλεκτρικής τομογραφίας για διάφορες διατάξεις ηλεκτροδίων.

Εκτεταμένα πειραματικά σετ δεδομένων προτείνουν ότι όλες οι διατάξεις ηλεκτροδίων μπορούν να μετρηθούν αποτελεσματικά όταν η πυκνότητα των οριζόντιων σχισμών των πλαστικών γεωτρήσεων είναι σχετικά υψηλή (μεγαλύτερη από 5 σχισμές/ηλεκτρόδιο). Ωστόσο, καθώς η πυκνότητα σχισμών αυξάνεται τα αποτελέσματα αντιστροφής των διατάξεων ηλεκτροδίων, που χρησιμοποιούν ηλεκτρόδιο ρεύματος και δυναμικού στην ίδια γεώτρηση (π.χ. πόλου-τριπόλου, διπόλου-διπόλου), υπέφεραν από σοβαρές ανωμαλίες. Σε μια τέτοια περίπτωση, μόνο η πόλου-διπόλου διάταξη μπορεί να χρησιμοποιηθεί αποτελεσματικά.

Τα παραπάνω συμπεράσματα εξετάστηκαν ακόμη σε πραγματικά δεδομένα πεδίου. Συγκεκριμένα, δεδομένα μετρήσεων ηλεκτρικής τομογραφίας συλλέχθηκαν μεταξύ πλαστικών στελεχών γεωτρήσεων παρακολούθησης, τοποθετημένες κατά μήκος της γραμμής του μετρό της Θεσσαλονίκης, το οποίο είναι υπό κατασκευή. Επίσης, προτάθηκαν επιπρόσθετες στρατηγικές μέτρησης μεταξύ γεωτρήσεων για να αντιμετωπιστεί η περιορισμένη ανάλυση της γεωηλεκτρικής απεικόνισης του υπεδάφους, εξαιτίας της μεγάλης απόστασης των γεωτρήσεων, είτε ενσωματώνοντας επιφανειακές μετρήσεις ηλεκτρικής τομογραφίας στα δεδομένα μετρήσεων ηλεκτρικής τομογραφίας μεταξύ

γεωτρήσεων, είτε εφαρμόζοντας μετρήσεις ηλεκτρικής τομογραφίας μεταξύ γεώτρησης και επιφάνειας.

Μερικά στελέχη γεωτρήσεων είχαν άγνωστο (αλλά χαμηλής πυκνότητας) αριθμό σχισμών ενώ κάποιες καινούργιες γεωτρήσεις κατασκευάστηκαν με μεγάλη πυκνότητα σχισμών. Τα αποτελέσματα αντιστροφής επιβεβαίωσαν τα πειραματικά ευρήματα: σε γεωτρήσεις χαμηλής πυκνότητας σχισμών μόνο οι διατάξεις ηλεκτροδίων που δεν χρησιμοποιούν τα ηλεκτρόδια ρεύματος και δυναμικού στην ίδια γεώτρηση παράγουν αποδεκτά αποτελέσματα, ενώ όλες οι διατάξεις δείχνουν να παράγουν καλά δεδομένα στην περίπτωση όπου η πυκνότητα των σχισμών είναι μεγάλη.

Όλα τα δεδομένα της εργασίας, πειραματικά και πεδίου, έδειξαν ότι οι μετρήσεις ηλεκτρικής τομογραφίας μεταξύ διάτρητων PVC γεωτρήσεων παρακολούθησης είναι εφικτές. Η εφαρμοσιμότητα τους εξαρτάται από την πυκνότητα των σχισμών, καθώς όσο μεγαλύτερη η πυκνότητα τόσο καλύτερη η ποιότητα δεδομένων. Μεταξύ των διατάξεων ηλεκτροδίων που εξετάστηκαν, η πόλου-διπόλου διάταξη (όπου το ηλεκτρόδιο ρεύματος δεν είναι στην ίδια γεώτρηση με τα ηλεκτρόδια δυναμικού) είναι η περισσότερο προτινώμενη διάταξη. Τα παραπάνω παρέχουν μια νέα προοπτική στην γεωηλεκτρική διασκόπηση καθώς όπως φαίνεται μπορούν να χρησιμοποιηθούν σε διάτρητα PVC στελέχη γεωτρήσεων μειώνοντας με αυτόν τον τρόπο το κόστος και τη δυσκολία της έρευνας.

CONTENTS

Table of figures

CHAPTER 1

Introduction

1.1 Thesis objectives

The development of cross-hole electrical resistivity tomography (ERT) is a powerful tool for obtaining higher resolution resistivity images of the subsurface compared to surface arrays, as the electrodes are placed closer to the possible targets of interest. Therefore, the cross-hole ERT method is widely applied for studying various geophysical problems, such as geological, hydrogeological, engineering and environmental (Goes and Meekes, 2004).

However, an issue of concern in cross-hole ERT surveys is, the so-called borehole effect, which is mainly due to the contrast between the borehole fluids and the host formation. The borehole effect can locally distort the electrical and measured potential fields (Doetsch et al., 2010), as the current produced by an electrode pole within the borehole is preferentially propagating inside the low resistivity fluid, ignoring the high resistivity host formation. This effect is rarely considered for the acquisition and analysis of the data, leading to image distortions and consequently to misinterpretations.

This work mainly focuses on the application of cross-hole ERT measurement tests in in plastic PVC cased slotted observation boreholes, by inserting a multi-electrode cable directly into the borehole. The borehole-casing act as a barrier to the current flow, resulting in extremely high apparent resistivity values. Therefore, the presence and density of slots in the PVC casing is critical for the measurement quality. Moreover, as the results seem to be highly affected by the electrode array used to obtain measurements, the study also focuses on comparing the effectiveness of different measuring schemes. More specifically, a water tank was used for performing measurement tests using various electrode arrays and different PVC casings, with a varying number of slots.

The findings of the experimental measurement tests were also cross-validated by performing several field cross-hole ERT measurement tests, using available water-level monitoring boreholes within the city of Thessaloniki, Greece. Moreover, additional field measurement tests, with different measuring schemes were carried out, to reinforce the measurement quality between boreholes.

1.2 Thesis outline

The content of the present study is briefly described below, for each chapter separately:

Chapter 2 introduces the basic theory of the electrical resistivity method presenting the electrical resistivity tomography (ERT) and its application between boreholes. A short description of the solution of the forward problem using the Finite Element Method is provided, along with a description of the inversion process.

Chapter 3 presents the methodology followed, starting from the generation of the electrode configurations, and proceeding to the acquisition, processing and inversion of the acquired datasets.

Chapter 4 describes the design, set-up and employment of the experimental tests, carried out into a plastic tank filled with tap water and also, it describes the tested electrode configurations. The results of the forward modelling of all the arrays in a cross-hole mode are illustrated and discussed. The inverted results of the experimental datasets obtained from different arrays and with different modelling bodies, using three pairs of test PVC-tubes are presented. An evaluation of all the datasets is also provided in order to draw some general conclusions.

Chapter 5 presents the results of the field measurement tests that were collected between real water-level monitoring boreholes, located in the city of Thessaloniki, Greece. The inverted results of the field datasets were obtained from different locations and involve piezometers of various slot density. The field measurement tests include measurements between boreholes (cross-hole), measurements between borehole and surface (borehole-to-surface) and surface measurements.

Chapter 6 includes the concluding remarks, summarizing the results from the experimental and field measurement tests.

CHAPTER 2

Basic theory

This chapter focuses on the basic principles of the electrical resistivity method and cross-hole ERT method including the basic measuring principles, the usage of the apparent resistivity, the basic surface electrode arrays and the electrical resistivity tomography ERT method.

The operation of the cross-hole electrical resistivity tomography (ERT) method and its applicability for obtaining higher resolution resistivity images of the subsurface, compared to surface arrays is described in detail.

Finally, an approach to the solution of the forward and inverse geoelectrical problem provides the basic information required to understand the modelling and inversion procedures followed in this work.

2.1 Principles of electrical resistivity method

The electrical resistivity method deals with the measurement of the ability of rocks and minerals to resist electric current passage, the so-called resistivity, which is inherent to the material and does not depend on its geometrical characteristics. The distribution of resistivity provides the geoelectrical structure of the subsurface leading indirectly to the geological characterization of the subsurface as different materials exhibit different resistivity values.

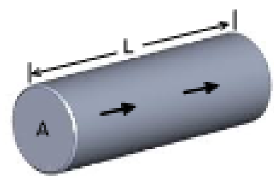

Figure 2.1: Conductor of length L and cross-section A.

In the case of a conductor (Fig. 2.1) with length L, cross-section A and Ohmic resistance R, the resistivity can be defined as the ratio of the product of Ohmic resistance R and cross-section A to length L, as expressed below:

$$\rho = \frac{RA}{L} \tag{2.1}$$

while the electrical conductivity, which is the reverse of resistivity, is defined as:

$$\sigma = \frac{1}{\rho} \tag{2.2}$$

The SI base unit of resistivity and conductivity is Ohm·m and Siemens/m respectively.

2.2 Electrical current propagation in homogeneous earth

2.2.1 Current electrode on the surface

To understand the process of electrical current's propagation within the earth, we consider the subsurface as a homogeneous medium of fixed resistivity (Fig. 2.2), where a positive electrical pole P (source), positioned on the surface, disperses electric current only in the subsurface, since the air has infinite resistance. At a long distance from the positive pole, a negative electrical pole is placed, closing the circuit.

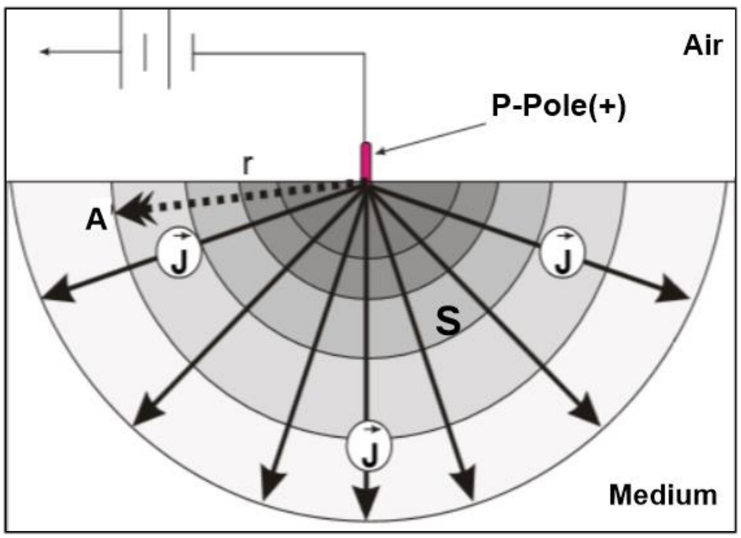

Figure 2.2: Electrical current propagation within homogeneous medium, by surface pole.

It is known that, the current density J is defined as the current intensity I per unit area of cross section area S.

$$J = \frac{I}{S} \qquad 2.3$$

According to Ohm's law, the current density can be written as the product of conductivity and electrical intensity.

$$J = \rho E \qquad 2.4$$

where, the current intensity is:

$$E = \frac{dV}{dr} \tag{2.5}$$

Combining equations 2.3, 2.4 and 2.5, the gradient of V can be defined as:

$$dV = \rho \left(\frac{I}{S}\right) dr \tag{2.6}$$

Considering that equipotential' shape is a hemisphere, the cross-section area S is equal to:

$$S = 2\pi r^2 \tag{2.7}$$

and solving equation 2.5 by integration, the potential V in a point A of distance r from pole P, is found:

$$V = \frac{\rho I}{2\pi r} \tag{2.8}$$

2.2.2 Current electrode on the subsurface

In the case where, one of the source's poles is within the subsurface (Fig. 2.3), e.g. into a borehole, the cross-section area of equipotential lines is equal to the cross-section of a sphere:

$$S = 4\pi r^2 \tag{2.9}$$

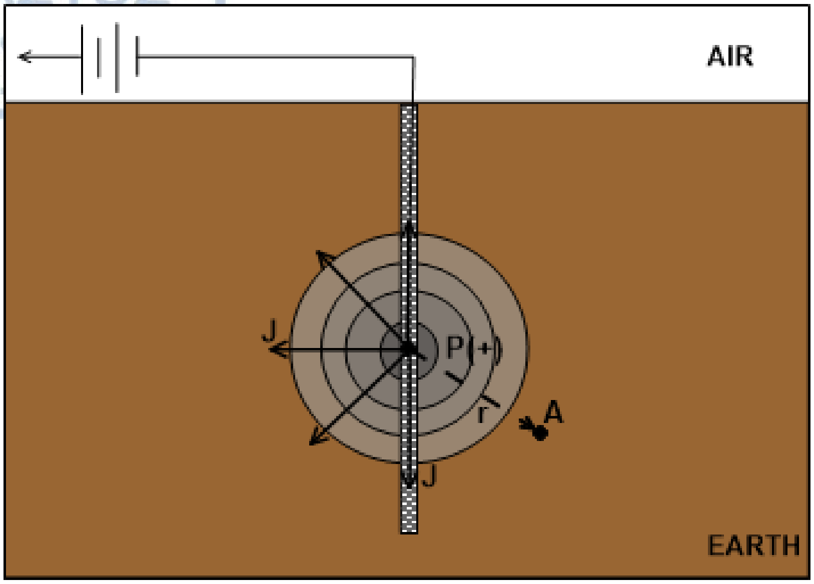

Figure 2.3: Electrical current propagation within homogeneous earth, by electrode in the subsurface.

Following the same procedure as in the previous case where the source was on the surface, the potential V in a point A at a distance r from the electrical pole when the last one is in the subsurface is defined as:

$$V = \frac{\rho I}{4\pi r} \qquad 2.10$$

It is known that the potential is a scalar quantity, hence the potential V of a point A (e.g. placed on the subsurface), can be represented as the result of the algebraic sum of several electrical poles, as expressed below:

$$V = (\frac{\rho}{4\pi})(\frac{I1}{r1} + \frac{I2}{r2} + \cdots + \frac{In}{rn}) \qquad 2.11$$

where r1, r2,.., rn, are the distances of the current sources from the pole.

2.2.3 Basis of resistivity method

The electrical resistivity method typically uses 2 pairs of electrodes, the first pair for the injection of the electric direct current into the ground, in the form of an alternating square wave with typical periods/cycle times of 0.5-2 sec. The second pair is used for the measurement of the potential difference (ΔV), as seen in Fig. 2.4. The potential (V) for a homogeneous earth at each point M and N is given by:

$$V_M = (\frac{\rho}{2\pi})(\frac{I}{AM} - \frac{I}{BM}) \quad 2.12$$

$$V_N = (\frac{\rho}{2\pi})(\frac{I}{AN} - \frac{I}{BN}) \quad 2.13$$

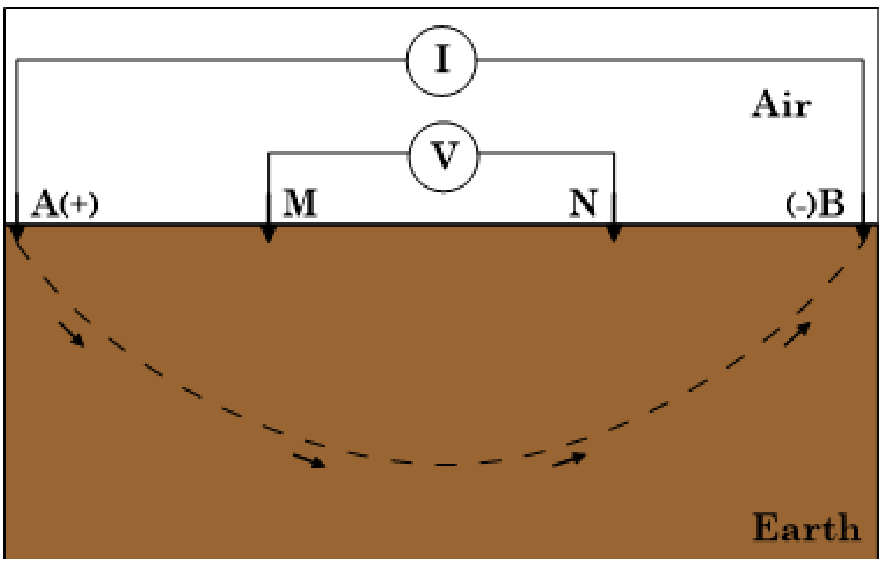

Figure 2.4: The main geometry of electrodes used by the electrical method. (After Tsourlos, 1995)

The potential difference (ΔV) between points M and N can be used to obtain the resistivity ρ of earth, which is defined as:

$$\rho = \left(\frac{2\pi \Delta V}{I}\right)\left(\frac{1}{\left(\frac{1}{AM} - \frac{1}{MB} - \frac{1}{AN} + \frac{1}{BN}\right)}\right) \quad 2.14$$

The second part of the equation 2.14 is the so-called geometrical factor, which is determined by the electrode array configuration, namely the spatial setup of the electrodes. It is obvious that the geometrical factor plays an important role for the calculation of the resistivity distribution within the subsurface.

2.3 Apparent resistivity

As mentioned above, the electrical resistivity method seeks to determine the resistivity ρ of the rocks and minerals by the injection of an electrical current through two electrodes and the measuring of the potential difference between two additional electrodes.

The electrical resistivity property is related to a homogeneous medium of fixed resistivity but as earth is heterogeneous the measured geoelectrical property does not correspond to a single material but reflects the bulk property of the materials in the surveyed area.

Thus, taking into account that earth is heterogeneous lead to the introduction of the term of apparent resistivity ρ_a, which is the measured quantity obtained in geoelectrical surveys and is calculated from:

$$\rho_a = \left(\frac{\Delta V}{I}\right) K \qquad 2.15$$

This quantity is not representative of the true resistivity of the materials in the earth, but, it is a normalization for any given electrode array configuration (e.g. Ward, 1990).

2.4 Basic resistivity arrays

The selection of the appropriate electrode configuration mainly depends on the aim of the geoelectrical prospecting, especially the depth and the size of the target of interest. Theoretically, the electrodes can be placed anywhere, as long as their positions are taken into account for the calculation of the geometrical factor.

Each electrode array configuration exhibits a different sensitivity and resolution capacity as well as different signal-to-noise ratio. Some of the basic and most common surface geoelectrical arrays are described below:

Wenner array: This is the simplest electrode array, where the potential pair of electrodes M, N is positioned between the current electrodes A,B (Fig. 2.5a). The distance between all electrodes is equal to a. The apparent resistivity for the Wenner array is calculated by the following relation:

$$\rho_a = 2\pi \mathrm{a} \left(\frac{\Delta V}{I}\right) \tag{2.16}$$

where the first part (2πa) is defined as the geometrical factor, with electrodes spacing a. Wenner array presents good signal to noise ratio and a good resolution to detect layered structures.

Schlumberger array: This electrode array is similar to Wenner array, where the potential electrodes are also positioned between current electrodes. However, the distance between the current electrodes is generally much longer than the distance between the potential electrodes (Fig. 2.5b). Supposing that the distance between current electrodes is

2L and the distance between potential electrodes is 2l, with L>10l, then the apparent resistivity is:

$$\rho_a = \left(\frac{\pi(L^2)}{2l}\right)\left(\frac{\Delta V}{I}\right) \qquad 2.17$$

The Schlumberger array has a good signal to noise ratio and is quite sensitive to delineate layered structures.

Dipole-Dipole array: In this electrode array, the potential and current electrodes are separated and the distance of each dipole is constant and equal to a. (Fig. 2.5c). The distance between both is na (n=1,2…) i.e. an integer multiple of the distance a. The apparent resistivity can be expressed as:

$$\rho_a = \left(\frac{\Delta V}{I}\right)\pi a n(n+1)(n+2) \qquad 2.18$$

The Dipole-dipole array is very sensitive in detecting lateral resistivity variations but suffers from a low signal-to-noise ratio. Its investigation depth depends on the distance between current and potential dipoles.

Pole Dipole array: This array is similar to Schlumberger array, where the potential dipole is positioned between the current electrodes, with the difference that one of the current's electrodes is placed in an "infinite" (i.e. very large) distance from the remaining electrodes, as shown in Fig. 2.5d. The apparent resistivity can be expressed as:

$$\rho_a = \frac{\left(\frac{\Delta V}{I}\right)(2\pi \mathrm{a} b)}{b - \mathrm{a}} \qquad 2.19$$

This array has a good vertical and horizontal resolution, as well as a good signal to noise ratio (better than the dipole-dipole but worse than the Schlumberger), while its main disadvantage is that it requires the use of a remote ("infinite") electrode.

Pole Pole array: The distance between a current and a potential electrode is α, while the remaining two electrodes are placed at infinite distance (Fig. 2.5e). The geometrical factor of pole pole array is $K = \frac{1}{a}$, similar to the Wenner electrode array, while the apparent resistivity is equal to:

$$\rho_a = 2\pi a \left(\frac{\Delta V}{I}\right) \qquad 2.20$$

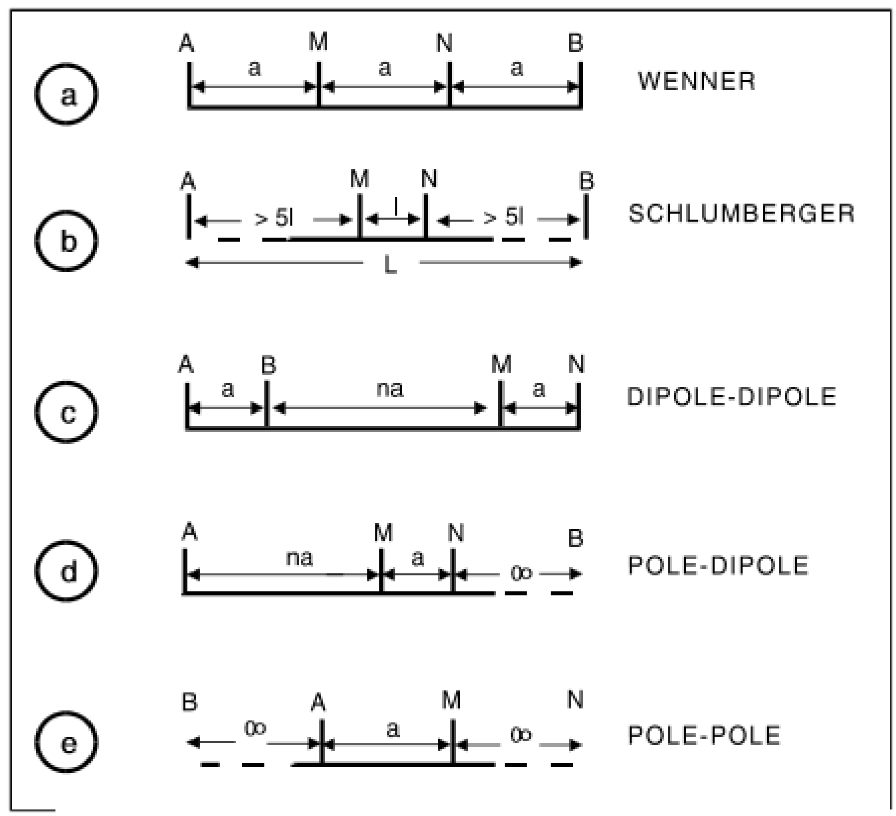

Figure 2.5: Basic resistivity arrays: a) Wenner, b) Schlumberger, c) Dipole-Dipole, d) Pole-Dipole, e) Pole-Pole (Tsourlos, 1995).

While geoelectrical arrays are related to the way that 4 electrodes are positioned on the ground during the geoelectrical survey the electrode arrays are not static but are moving in order to survey the specified area. The ways the electrodes are moved during a survey are described as geoelectrical survey modes. For surface surveys there are three different modes in electrical resistivity method, namely, the 1D lateral profiling (Fig. 2.6a), dedicated to detect only lateral variations in resistivity, the 1D vertical electrical sounding (Fig. 2.6b), useful for the detection of changes of resistivity with depth, and lastly, the 2D electrical resistivity tomography (ERT) which is a composition of the first two and provides a more realistic imaging of the subsurface structure in two dimensions.

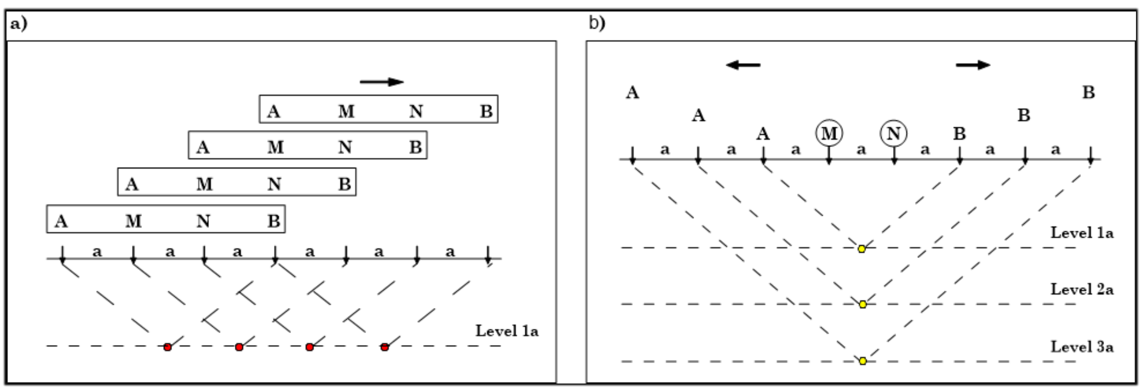

Figure 2.6: One dimensional electrical resistivity modes. a) Electrical lateral profiling, b) Electrical sounding.

2.5 Electrical resistivity tomography

The electrical resistivity tomography (ERT) can be considered as the natural evolution of the standard geoelectrical method. The advent of fully automated measuring instruments (e.g. Griffiths et al., 1990), with electrode multiplexing ability in combination with the development of advanced interpretation algorithms allows the collection of a large amount of data (Fig.2.7) and the production of reliable electrical resistivity images of the subsurface (Barker, 1981; Auken et al., 2006).

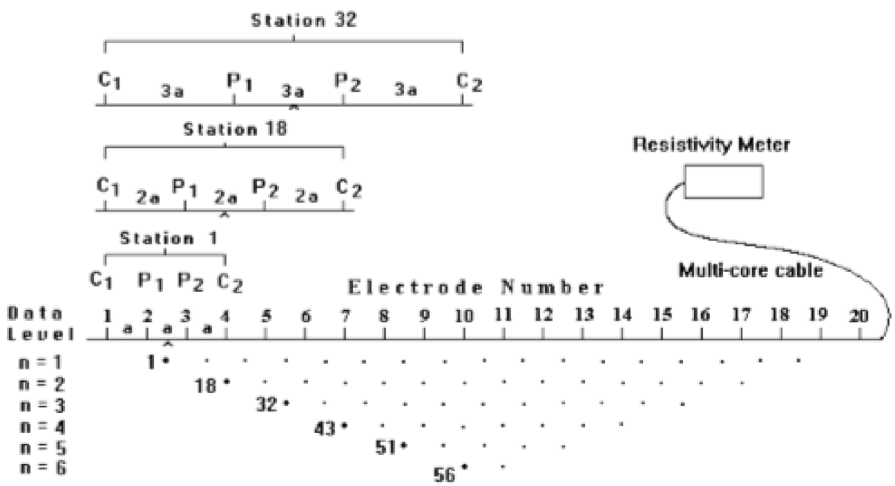

Figure 2.7: Sequence of measurements of electrical resistivity tomography (ERT).

These significant technological advances, related to the resistivity data acquisition and analysis, improved dramatically the applicability of the geoelectrical method. First, the improvement of electrical resistivity instrumentation and specifically, the generation of multi-electrode resistivity measuring systems, reduced the acquisition time, increasing significantly at the same time, the amount of measured data and subsequently the resolving ability of the measured data sets. Moreover, the development of powerful mathematical algorithms, enhanced the resistivity data processing and analysis, allowing the conversion of the apparent resistivity data into true resistivity subsurface distributions through the inversion process.

As a result, the ERT technique can reliably reconstruct the geoelectrical subsurface structure, either in two or in three dimensions. The Electrical Resistivity Tomography (ERT) technique is currently considered one of the most important geophysical tools for imaging the subsurface structure. The application of ERT has particularly wide use for environmental monitoring involving (among others) groundwater exploration, mapping of fractured aquifers, monitoring transport processes of contaminants etc.

2.6 Cross-hole ERT method

The development of cross-hole electrical resistivity tomography (ERT) is a powerful tool for obtaining higher resolution resistivity images of the subsurface in comparison to surface arrays as the electrodes are placed closer to the possible targets. The cross-hole ERT is widely applied for studying various geophysical problems, such as geological, hydrogeological, engineering and environmental (Goes and Meekes, 2004, Wilkinson et al., 2009, etc.). The availability of boreholes near the investigation area is the only feasible way to access the subsurface for the realization of cross-hole electrical resistivity tomography.

The process of cross-hole electrical resistivity tomography (ERT) is achieved through the insertion of multi-electrode cables directly into two (or more) boreholes. In case of a single borehole, the borehole electrodes can be used in combination to surface ones to obtain the borehole-to-surface measurements. The boreholes are usually filled with water, providing galvanic contact between the electrodes and the surrounded host formation. In some cases, where the boreholes are filled with air, the contact between the electrodes and the host formation can be realized either by incorporating first the electrodes outside the borehole-casings and then lower them down and sticking to the borehole wall providing sufficient electrical contact with the host formation, or by filling the borehole with mud or moist soil.

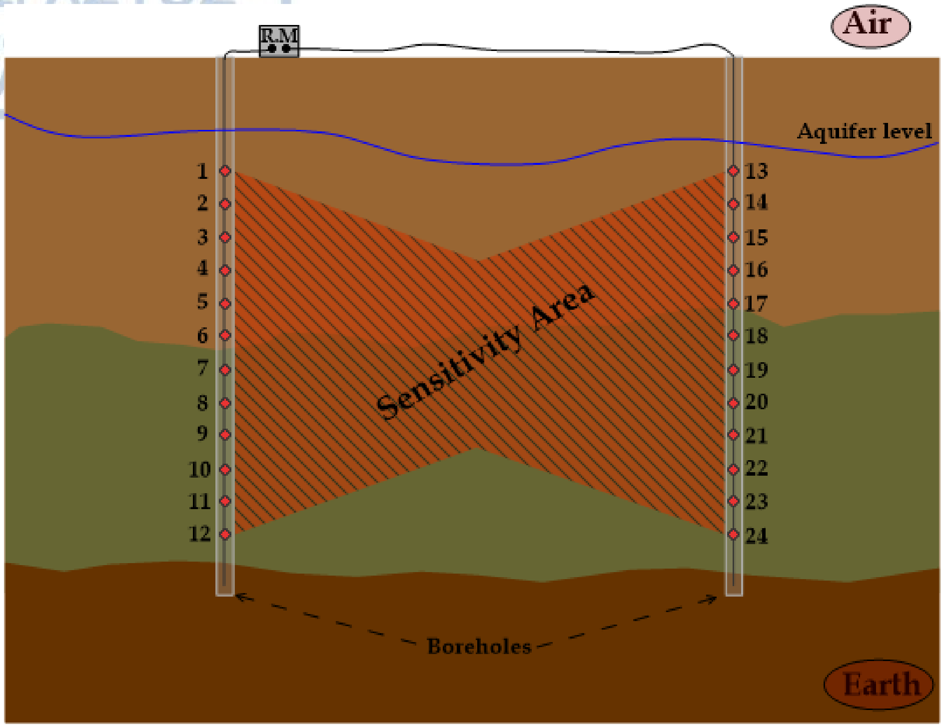

Figure 2.8: A schematic cross-hole electrical resistivity tomography (ERT) arrangement and its sensitivity area.

In cross-hole ERT surveys the electrode measurement schemes can follow the general pattern of the surface surveys adjusted to the borehole environment or can be significantly differentiated. Several electrode arrays have been proposed for cross-hole ERT surveys, including pole-pole (Daily and Owen 1991; Shima 1992), pole-tripole (Goes and Meekes 2004, Leontarakis and Apostolopoulos, 2012, 2013), bipole-bipole (Bing and Greenhalgh 1997) and pole-bipole (Bing and Greenhalgh 1997, 2000). In this study, the last three configurations of electrodes are used and hence, they will be described in more detail in a following chapter.

An issue of concern in cross-hole ERT surveys is the influence of the various borehole effects to the resistivity data (Doetsch et al. 2010). The main borehole effect is the so-called borehole-fluid effect (Doetsch et al. 2010), which is mainly produced due to the contrast between host formation and borehole fluids. This effect can locally distort the electrical and measured potential fields (Osiensky et al., 2003; Doetsch et al., 2010, Cho et al., 2016), as the current produced by an electrode pole within the borehole is preferentially propagating inside the low resistivity fluid, ignoring the high resistivity host formation. In cross-hole ERT surveys, this effect is rarely considered for the acquisition and analysis of the data, leading to image deformations and consequently to misinterpretations. Several cross-hole ERT studies have been carried out to find out the causes of this effect.

Nimmer et al., (2008) and Doetsch et al., (2010) indicated that the borehole-fluid effect is closely related to the geoelectrical property contrast between the borehole fluid and the host formation, and to the borehole diameter, while they showed that conventional 2.5D inversion algorithms cannot model appropriately the resultant resistivity distribution, as the borehole effect is clearly a three-dimensional one (Cho et al., 2016). Borehole inversion effects intensify when the borehole diameter or the contrast between the borehole fill and the host formation increase (Nimmer et al., 2008) and are more important to the shorter bipole spacings (Doetsch et al., 2010).

One of the constraints of cross-hole ERT is that, satisfactory results normally can only be obtained when the aspect ratio (hole depth/ hole separation) is limited (e.g. less than 1.5) (Ramirez et al., 1995). Thus, it is quite common that, practically, cross-hole electrical tomography cannot be applied always, due to the wide spacing that exists between adjacent boreholes (when cross hole ERT measurements are not predicted). In this case, the complementary use of surface electrodes, can improve the resolving ability of the cross-hole configuration.

2.6 Forward modelling

The process to compute a theoretical dataset (potentially observable from real measurements) from an appropriate set of model parameters is typically described as the forward modelling problem. In the case of electrical resistivity method, the forward modelling is used to obtain the apparent resistivity distribution from a known geoelectrical model.

Specifically, forward modelling solves the differential Poisson's equations (eq. 2.21, 2.22), that rule the electrical current's flow in the ground (e.g. Telford et al., 1976, 1991) approximating the apparent resistivity distribution that would be measured by a real geoelectrical survey.

$$\nabla\varphi(x,y,z) = -\rho(x,y,z)\cdot J(x,y,z) \qquad 2.21$$

$$\nabla J(x,y,z) = I_s(x,y,z) \qquad 2.22$$

In the above equations, φ and J is the electrical potential and current density respectively, around a point source I, and ρ is the electrical resistivity distribution within the earth.

The solution of forward modelling is typically approached by two families of methods, depending on the complexity of the investigated structures:

- Analytical methods
- Numerical methods

Analytical methods typically deal with simple geometries of the geological structures of the subsurface, while by contrast numerical methods deal with more complicated rock formations of irregular shape and boundaries. It is obvious that the numerical methods are widely used for the solution of forward modelling due to the possibility to realistically model the complexity of the subsurface.

The numerical methods are separated to integral equation methods and differential equation methods. The most common numerical method used to solve the forward problem is the so-called Finite Element Method (Mufti 1976; Dey and Morisson, 1979), which simplifies the subsurface to isotropic cells and simulates the earth's topography in order to solve the resistivity forward problem.

Although, a 3-D approach is the most realistic imaging of the earth's subsurface, the complicated algorithms which are required to solve three-dimensional equations of a very large number of measurements and the difficulty of accomplishing three dimensional measurements in the field, render 3-D interpretation too complicated. On the other hand, a 2-D modelling approach which considers that the current's flow and subsurface resistivity vary in two dimensions, is quite simple and often efficient to illustrate earth's subsurface in detail. Therefore, in this work a 2.5-D modelling approach is employed, where the subsurface resistivity varies in two dimensions regarding the geometry of investigation area, while the electrical current "flows" in all three dimensions.

2.7 Inversion of ERT data

ERT Inversion is the opposite process of forward resistivity modelling, namely the procedure of finding an approximate resistivity distribution within the earth, given the observed data (i.e. measured potential differences, Fig. 2.9).

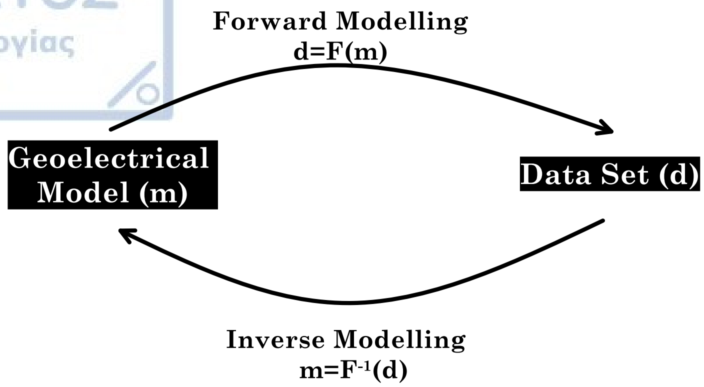

Figure 2.9: Forward and Inverse modelling procedure.

Many attempts have been made to interpret resistivity data, initially for structures of simple geometry, by using analogue and analytical methods (e.g. Telford et al., 1976, 1991). With the improvement of computer technology, inversion algorithms were introduced to solve more complicated geophysical problems (Wiggins 1972, Jackson 1972).

The one-dimensional resistivity inversion was introduced by Ward and Glenn (1976), based on the generalized linear inverse theory, by Inman et al (1973) and considering only vertical resistivity variations. Later, two-dimensional resistivity methods using numerical modelling techniques (Madden 1967, Jespen 1969, Lee 1975), were used to interpret resistivity data in terms of two-dimensional geological structures (see Narayan et al., 1994). Pelton et al (1978) were the first to develope an algorithm capable to invert 2D resistivity and induced-polarization data and since then, many other workers improved the resistivity inversion by applying several techniques (Smith and Vozoff 1984, Tong and Yang 1990, etc.). In the following we provide a summary description of the ERT inversion procedure.

In the case of linear problems, the solution of inverse problem is easy to be determined, however in the geoelectrical inverse problem the model parameters and the data set are related in a non-linear manner, hence the solution of the inverse problem requires an iterative approach (Tarantola, 1987).

This solution can be obtained by transforming the problem to a linear one, after the discretization of the model (investigation) area using a Taylor series expansion, in order to relate the model parameters perturbations (with respect to an initial model) to the data set in the following form:

$$dy = J \cdot dx \qquad 2.24$$

where, dy is a vector containing the differences between the observed and calculated data, dx is the approximate correction of the model parameters vector (with respect to an initial model) and J is a matrix composed of the partial derivatives of data set with respect to the model parameters (at the initial model), known as the Jacobian matrix (Loke and Barker, 1995) or stiffness matrix (Fig. 2.10). Its element is given by the equation:

$$J_{ij} = \frac{\partial d_i}{\partial \sigma_j} \qquad 2.25$$

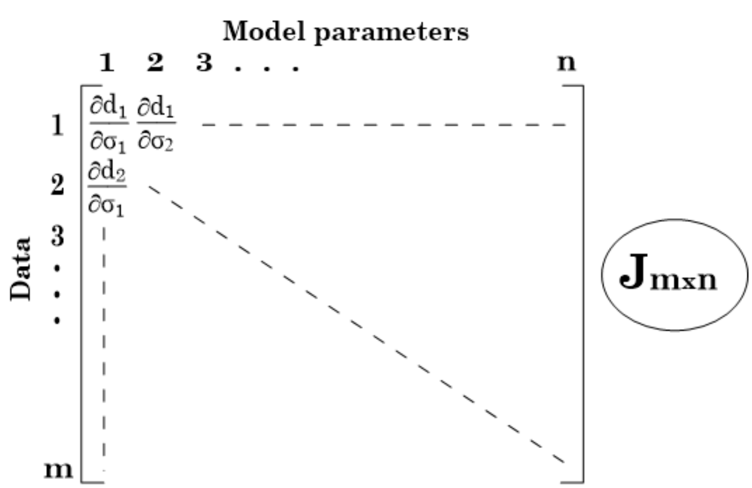

Figure 2.10: Jacobian matrix of m-number of data and n-number of model parameter.

The Jacobian matrix, which is an important factor to the solution of the inverse problems, is also referred as sensitivity matrix since it produces a metric of the sensitivity of the observed data to small changes of the subsurface resistivity (Tsourlos, 1995). The Jacobian matrix is calculated within the process of the forward modelling solver.

As the geoelectrical inverse problem is generally ill posed, several methods that stabilize the inversion procedure have been proposed. The most popular inversion technique is the smoothness-constrained inversion (Tikhonov, 1963; Constable et al, 1987). According to this technique, smoothness constraints are incorporated into the inversion algorithm calculating the resistivity correction at every iteration as follows:

$$dx = (J^T J + \mu C^T C)^{-1} * J^T * dy \qquad 2.26$$

and hence, the new resistivity estimation is given by:

$$x_{new} = x_{old} + d_x \qquad 2.27$$

where C is the smoothness matrix, which forces the computed parameters being close to each other and μ is the Lagrangian multiplier, which controls the resolution and stability of the inverse problem.

The smoothness constraint allows the computed parameters to be smooth in space imposing stability to the solution of the equation 2.24 and producing a model which is a reasonable representation of the subsurface (Tsourlos, 1995). This smoothness constraint is defined by the roughness term (Constable et al., 1987) and determines the degree of smoothness constrained minimization of the computed model.

As earlier described, an initial model of resistivity distribution needs to be adopted, usually a homogeneous one, which is usually discretized in many nodes that simulate the model parameters, for which an initial value of resistivity or conductivity is defined at each block. By solving the forward problem for these model responses, the theoretical model data are calculated, to be compared with the observed data. The error between the calculated and observed data is the model misfit or data misfit and is expressed by the Root Mean Square (RMS). This RMS error determines the convergence of the algorithm or the repetition of the process, re-resolving the forward problem with corrected resistivity estimations, until the RMS error reaches to an acceptable level (Fig. 2.11).

The geoelectrical inversion algorithm seeks iteratively to compute an improved model by simultaneously minimizing the roughness of the model and the data misfits (RMS error) between the observed and calculated data that correspond to the model. To achieve the best possible minimization of the model roughness, in this work, the L2-norm criterion is used, which minimizes the sum of squares of the model resistivity values. On the other hand, for the minimization of the data misfits the L1-norm criterion (Ellis and Oldenburg, 1994) is used in this work, which minimizes the sum of absolute differences between the observed and calculated data, reducing the effect of data outliers as it has been reported by several researchers (Farquharson and Oldenburg, 1998; Menke, 1989, Loke and Dahlin, 2003).

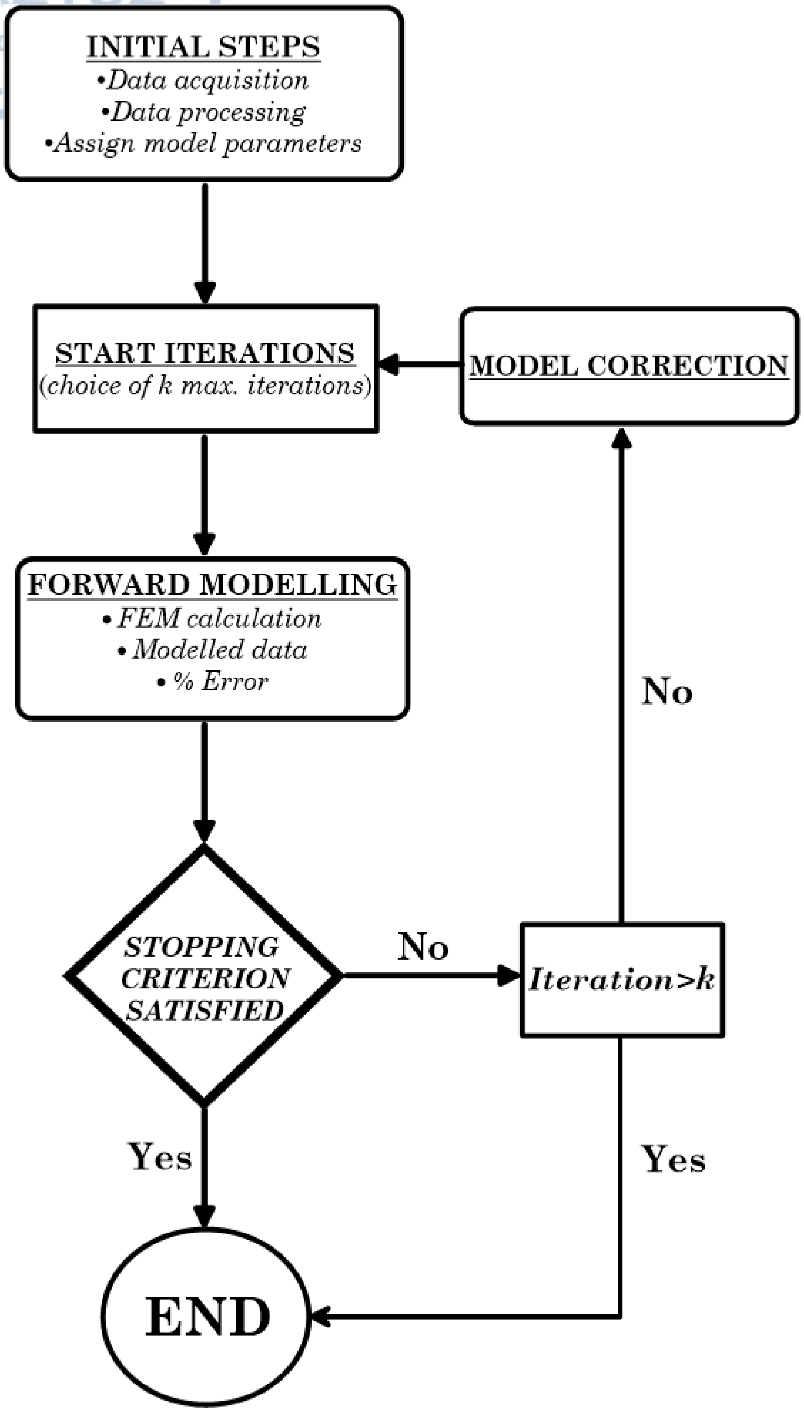

Figure 2.11: Flow chart of Inversion scheme.

CHAPTER 3

Tools and methods

The following chapter presents the geoelectrical resistivity tools and methods that were used in this work and are required for the ERT data acquisition, processing and analysis.

Initially, this chapter focuses on the protocol generating scheme for obtaining cross-hole and borehole-to-surface ERT measurements. The Matlab based protocol generation program, which was developed in the framework of this work, is presented and its details are explained.

Additionally, the measurement set-up and instrumentation as well as the tools for the processing of the experimental and field data acquired in this work are presented and explained together with the DC2DPRO software that was used to produce the inverted images of the "true" subsurface resistivity distribution.

3.1 Protocol Generating Algorithm

A special algorithm (CrosProOpt, Almpanis (c) 2018) was developed in Matrix Laboratory (MATLAB) language to generate full cross-hole measurement protocols compatible with any cross-hole geometry and electrode positions, producing files ready to be employed by the measuring instrument used in this work (Syscal Pro resistivity meter, Iris Instruments).

Although, the main function of this algorithm is the generation of cross-hole measurement protocols, further utilities were incorporated such as the generation of the equivalent optimum protocols, the conversion of the acquired cross-hole resistivity data to be compatible form with the DC2DPRO inversion software (Kim, 2013) and lastly the generation of borehole to surface measurement protocols. All previous items are discussed in detail in the following. Note that an effort was made to make the program user friendly. via a Graphical User Interface (GUI) module.

3.1.1 Cross-hole ERT Protocol generation

Initially, the generation of the cross-hole ERT measurement protocols demands some input parameters directly defined by the user, related to the cross-hole geometry survey, such as, the distance between boreholes, the interval spacing of the electrodes, the number and depth of the electrodes at each borehole and finally the electrode array configuration (Fig. 3.1).

Three different electrodes array configurations are supported by the CrosProOpt protocol generator algorithm, namely the bipole-bipole, pole-dipole and pole-tripole arrays. Although cross-hole ERT arrays are not as standardized as the surface ones, the above arrays were selected, as they are, the most widely used in literature (Bing, & Greenhalgh, 2000; Okpoli, 2013; Dahlin and Zhou, 2004) and have exhibited good characteristics in view of their resolving ability and signal strength.

To avoid obtaining measurements of low signal strength the user can filter-out some of the produced data points based on their geometrical factor. Finally, the protocol generator provides a list of options to export the measurement protocols to various file formats, such as the following:

- ***txt file****:* This option saves the number and the X, Z, coordinates of the electrodes, as well as the related electrode number-id for each measurement. This file is fully compatible with the Iris Instruments protocol format, so it can be directly imported into the resistivity meter used in this work.
- ***a2d file(Model)****:* Its format is similar to the previous file, by the difference that it is appropriate for performing forward modelling by the DC2DPRO inversion software (Kim, 2013).
- ***dat file(Model)****:* This file is supported by the RES2DINV inversion software (Loke, 2016) for forward modelling.

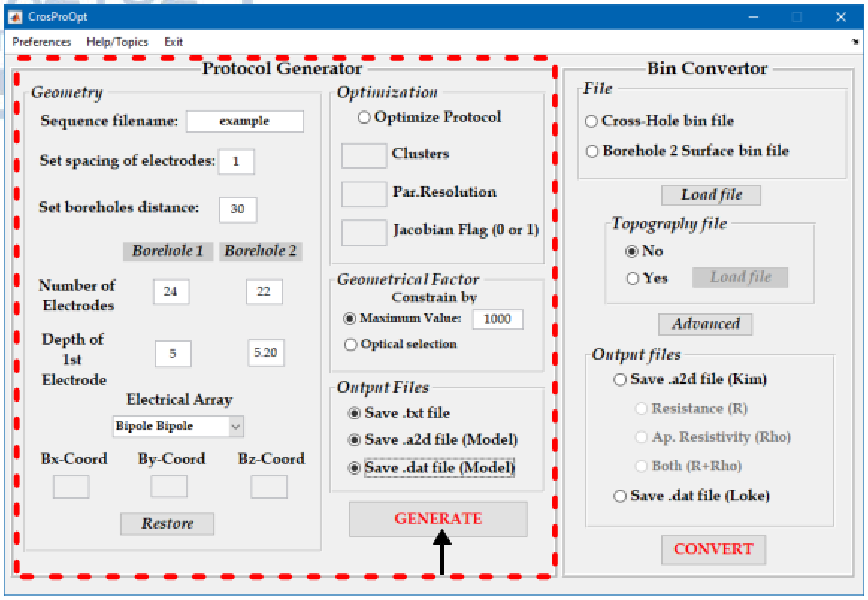

Figure 3.1: Generation of protocols, by CrosProOpt algorithm.

3.1.2 Optimization

Optimization of protocols is an additional option, provided by the CrosProOpt protocol generator developed in this study. The software seeks to produce an optimum protocol, with the best possible sensitivity pattern of the initial measurement protocol. The main advantage of the optimum protocol is the reduction to the total number of measurements and hence of the acquisition time, with no particular influence to the quality of the produced inversion results. The optimization method used in this work, is presented in detail in the work of Athanasiou et al., 2009 and so only a brief description of the optimization procedure will be given here.

The optimization method used in this work is based on the sensitivity matrix approach. The space corresponding to a selected electrode geometry and measuring protocol is separated into a set of parameters, the number of which is defined by the "Par. Resolution" option. The sensitivity value of every measurement with respect to the model parameter (i.e. "Jacobian matrix") is calculated. According to the selected number of clusters

("Clusters"), only the measurements exhibiting the highest sensitivity in relation to every parameter are included into the optimized data set. Finally, the optimized dataset is generated through an iterative procedure, selecting only these measurements that have the highest absolute value of sensitivity with respect to every parameter.

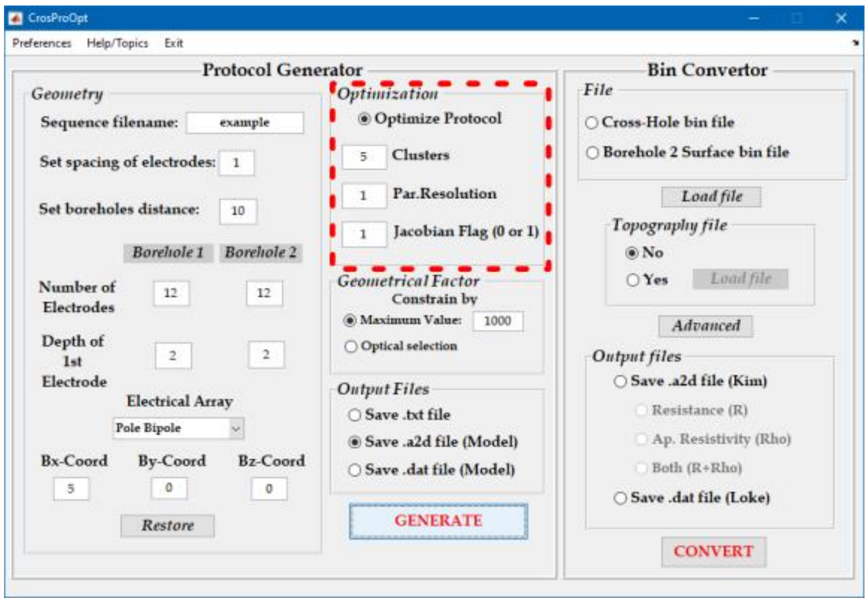

Figure 3.2: Protocol optimization option, provided by CrosProOpt algorithm.

In the case where the optimization process is selected (Fig.3.2), the protocol generator algorithm produces two protocols, a full data set measurement protocol and an optimum one. Figure 3.3, presents the inversion results of a synthetic full dataset measurement protocol (Fig. 3.3b) and an optimum one (Fig. 3.3c), for the case of a known resistivity distribution model, consisting of four resistive blocks of high resistivity (100 Ohm-m) into a low resistivity (10 Ohm-m) medium shown in Fig.3.3a.

Although, the optimized protocol has almost four times less measurements (470 data points) than the full one (1474 data points), it produces an inverted model which it practically identical to the one produced by the original protocol. The main advantage of using the optimized protocol is that the data acquisition time and the associated processing time is significantly reduced.

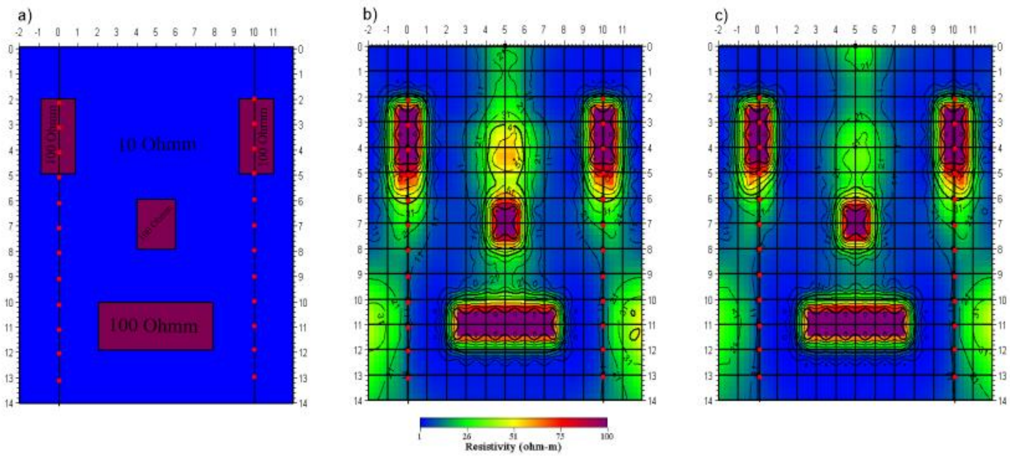

Figure 3.3: Forward modelling results for a full and optimum protocol: (a) resistivity distribution model (b) full protocol and (c) optimum protocol.

3.1.3 Conversion of data set

An additional option of the CrosProOpt algorithm, is the conversion of the collected data through the produced protocol files from the instrument .bin formats into data file formats compatible with widely used inversion software, such as DC2DPRO or the RES2DINV inversion software (Fig.3.4).

In this part of the algorithm, the user can also insert the exact topography information of the cross-hole survey geometry (i.e. x,y,z coordinates of the electrodes) and therefore can correct/modify various parameters such as the electrode spacing, borehole separation and electrode elevation. This option is also applicable to the borehole-to-surface measurements.

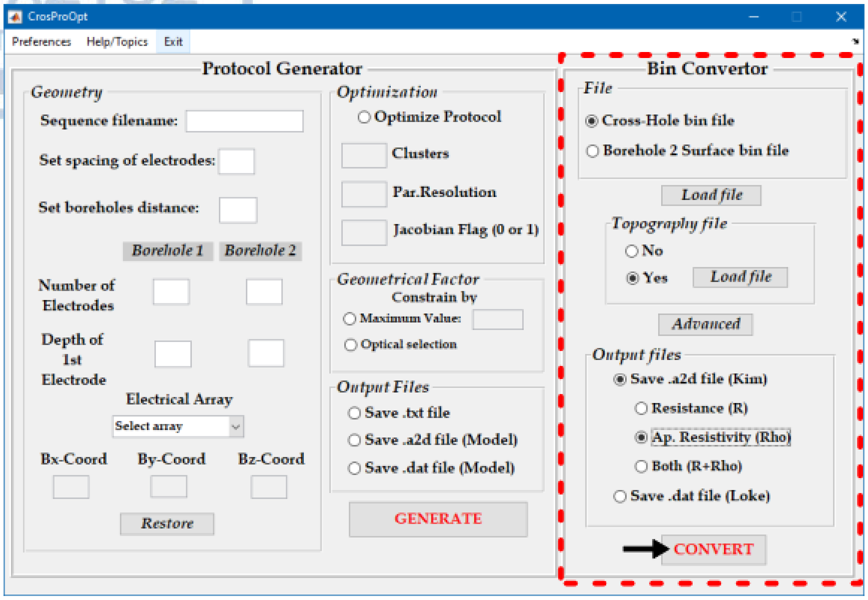

Figure 3.4: Conversion of Cross-hole or Borehole to Surface binary files provided by CrosProOpt algorithm.

3.1.4 Borehole-to-surface protocol

The generation of borehole-to-surface ERT measurement protocol, for simultaneous measurements between borehole and surface, is an additional function of the developed CrosProOpt module. This type of measurements can be used in the case of a single borehole or in the case that the distance between the adjacent boreholes is so long that the actual cross-hole measurements cannot provide adequate resolving ability, especially for the central area between boreholes.

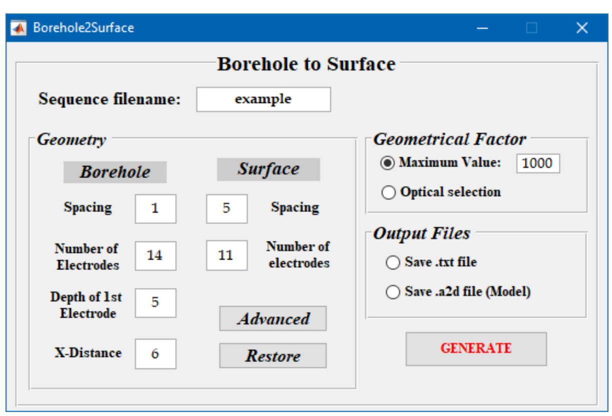

Figure 3.5: Generation of Borehole to Surface protocol, by CrosProOpt algorithm.

The generation of the borehole-to-surface ERT measurement protocols demands some input parameters directly defined by the user, related to the geometry survey, such as the interval spacing and the number of the borehole and surface electrodes, the depth of the 1st electrode at the borehole and the position of the borehole regarding the section that contains the surface electrodes (Fig. 3.5). The user can also reject some of the produced data points based on their geometrical factor, to avoid obtaining measurements of low signal strength. Finally, the borehole to surface protocol generator can export the measurement protocol as a “txt” file, that can be directly imported into the resistivity meter and as a “a2d” file, that can be used to perform forward modelling tests.

3.2 Data Acquisition and Processing

3.2.1 Resistivity meter

The resistivity meter used for both experimental and field data acquisition is the multi-channel and multi-electrode resistivity and induced polarization measuring system, Syscal Pro, manufactured by the IRIS instruments (Fig.3.6). The acquisition process is automatically realized, as long as, the instrument is supplied with the appropriate protocol.

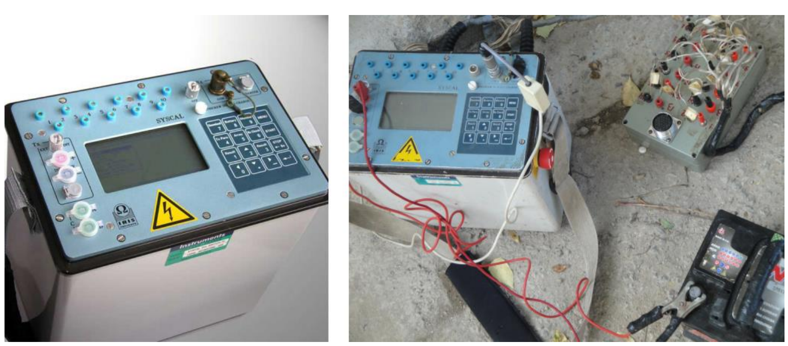

Figure 3.6: Syscal Pro resistivity meter (IRIS instruments).

Compared to standard ERT systems, this acquisition system can obtain fast data acquisition, since it can measure simultaneously up to 10 potential channels with a current single injection. The maximum current and potential source is 2.5 A and 800-1000 V, respectively. Moreover, the measurement precision is 0.2%, while the measurement resolution is as low as 1 μV. The particular instrument can address up to 48 electrodes automatically by using an integrated multiplexer module.

3.2.2 Prosys II

The Prosys II (Iris Instruments) resistivity data management software was used to download the acquired data from the resistivity meter (Fig.3.7). This software also provides a preliminary visualization, editing and processing of the resistivity data.

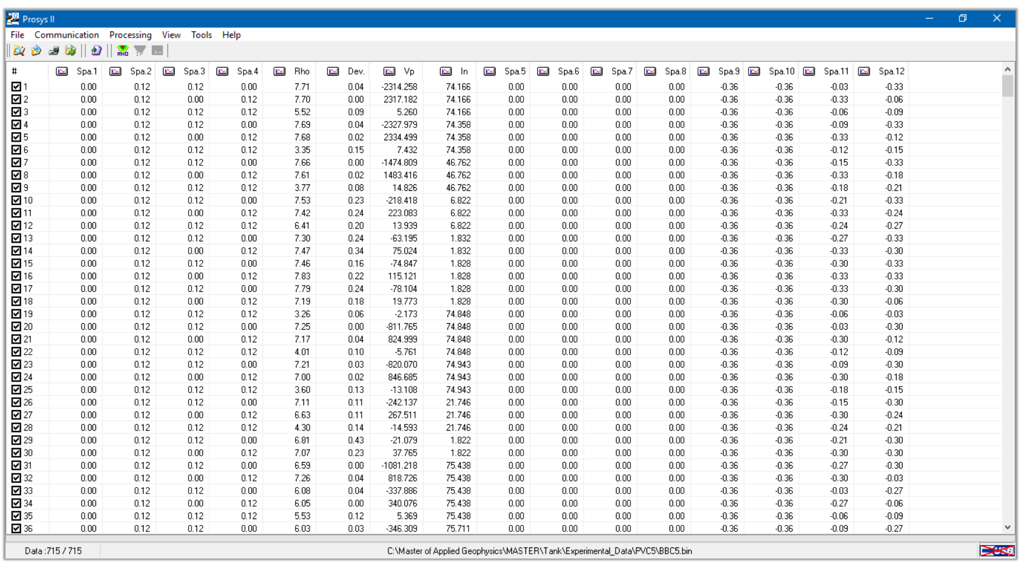

#	Spa.1	Spa.2	Spa.3	Spa.4	Rho	Dev.	Vp	In	Spa.5	Spa.6	Spa.7	Spa.8	Spa.9	Spa.10	Spa.11	Spa.12
1	0.00	0.12	0.12	0.00	7.71	0.04	-2314.258	74.166	0.00	0.00	0.00	0.00	-0.36	-0.36	-0.03	-0.33
2	0.00	0.12	0.00	0.12	7.70	0.00	2317.182	74.166	0.00	0.00	0.00	0.00	-0.36	-0.36	-0.33	-0.06
3	0.00	0.12	0.12	0.12	5.52	0.09	5.260	74.166	0.00	0.00	0.00	0.00	-0.36	-0.36	-0.06	-0.09
4	0.00	0.12	0.12	0.00	7.69	0.04	-2327.979	74.358	0.00	0.00	0.00	0.00	-0.36	-0.36	-0.09	-0.33
5	0.00	0.12	0.00	0.12	7.68	0.02	2334.499	74.358	0.00	0.00	0.00	0.00	-0.36	-0.36	-0.33	-0.12
6	0.00	0.12	0.12	0.12	3.35	0.15	7.432	74.358	0.00	0.00	0.00	0.00	-0.36	-0.36	-0.12	-0.15
7	0.00	0.12	0.12	0.00	7.66	0.00	-1474.809	46.762	0.00	0.00	0.00	0.00	-0.36	-0.36	-0.15	-0.33
8	0.00	0.12	0.00	0.12	7.61	0.02	1483.416	46.762	0.00	0.00	0.00	0.00	-0.36	-0.36	-0.33	-0.18
9	0.00	0.12	0.12	0.12	3.77	0.08	14.826	46.762	0.00	0.00	0.00	0.00	-0.36	-0.36	-0.18	-0.21
10	0.00	0.12	0.12	0.00	7.53	0.23	-218.418	6.822	0.00	0.00	0.00	0.00	-0.36	-0.36	-0.21	-0.33
11	0.00	0.12	0.00	0.12	7.42	0.24	223.083	6.822	0.00	0.00	0.00	0.00	-0.36	-0.36	-0.33	-0.24
12	0.00	0.12	0.12	0.12	6.41	0.20	13.939	6.822	0.00	0.00	0.00	0.00	-0.36	-0.36	-0.24	-0.27
13	0.00	0.12	0.12	0.00	7.30	0.24	-63.195	1.832	0.00	0.00	0.00	0.00	-0.36	-0.36	-0.27	-0.33
14	0.00	0.12	0.00	0.12	7.47	0.34	75.024	1.832	0.00	0.00	0.00	0.00	-0.36	-0.36	-0.33	-0.30
15	0.00	0.12	0.12	0.00	7.46	0.16	-74.847	1.828	0.00	0.00	0.00	0.00	-0.36	-0.36	-0.30	-0.33
16	0.00	0.12	0.00	0.12	7.83	0.22	115.121	1.828	0.00	0.00	0.00	0.00	-0.36	-0.36	-0.33	-0.33
17	0.00	0.12	0.12	0.00	7.79	0.24	-78.104	1.828	0.00	0.00	0.00	0.00	-0.36	-0.36	-0.33	-0.30
18	0.00	0.12	0.00	0.12	7.19	0.18	19.773	1.828	0.00	0.00	0.00	0.00	-0.36	-0.36	-0.30	-0.06
19	0.00	0.12	0.12	0.12	3.26	0.06	-2.173	74.848	0.00	0.00	0.00	0.00	-0.36	-0.36	-0.06	-0.03
20	0.00	0.12	0.12	0.00	7.25	0.00	-811.765	74.848	0.00	0.00	0.00	0.00	-0.36	-0.36	-0.03	-0.30
21	0.00	0.12	0.00	0.12	7.17	0.04	824.999	74.848	0.00	0.00	0.00	0.00	-0.36	-0.36	-0.30	-0.12
22	0.00	0.12	0.12	0.12	4.01	0.10	-5.761	74.848	0.00	0.00	0.00	0.00	-0.36	-0.36	-0.12	-0.09
23	0.00	0.12	0.12	0.00	7.21	0.03	-820.070	74.943	0.00	0.00	0.00	0.00	-0.36	-0.36	-0.09	-0.30
24	0.00	0.12	0.00	0.12	7.00	0.02	846.685	74.943	0.00	0.00	0.00	0.00	-0.36	-0.36	-0.30	-0.18
25	0.00	0.12	0.12	0.12	3.60	0.13	-13.108	74.943	0.00	0.00	0.00	0.00	-0.36	-0.36	-0.18	-0.15
26	0.00	0.12	0.12	0.00	7.11	0.11	-242.137	21.746	0.00	0.00	0.00	0.00	-0.36	-0.36	-0.15	-0.30
27	0.00	0.12	0.00	0.12	6.63	0.11	267.511	21.746	0.00	0.00	0.00	0.00	-0.36	-0.36	-0.30	-0.24
28	0.00	0.12	0.12	0.12	4.30	0.14	-14.593	21.746	0.00	0.00	0.00	0.00	-0.36	-0.36	-0.24	-0.21
29	0.00	0.12	0.12	0.00	6.81	0.43	-21.079	1.822	0.00	0.00	0.00	0.00	-0.36	-0.36	-0.21	-0.30
30	0.00	0.12	0.00	0.12	7.07	0.23	37.765	1.822	0.00	0.00	0.00	0.00	-0.36	-0.36	-0.30	-0.30
31	0.00	0.12	0.12	0.00	6.59	0.00	-1081.218	75.438	0.00	0.00	0.00	0.00	-0.36	-0.36	-0.27	-0.30
32	0.00	0.12	0.00	0.12	7.26	0.04	818.726	75.438	0.00	0.00	0.00	0.00	-0.36	-0.36	-0.30	-0.03
33	0.00	0.12	0.12	0.00	6.08	0.04	-337.886	75.438	0.00	0.00	0.00	0.00	-0.36	-0.36	-0.03	-0.27
34	0.00	0.12	0.00	0.12	6.05	0.00	340.076	75.438	0.00	0.00	0.00	0.00	-0.36	-0.36	-0.27	-0.06
35	0.00	0.12	0.12	0.12	5.53	0.12	5.369	75.438	0.00	0.00	0.00	0.00	-0.36	-0.36	-0.06	-0.09
36	0.00	0.12	0.12	0.00	6.03	0.03	-346.309	75.711	0.00	0.00	0.00	0.00	-0.36	-0.36	-0.09	-0.27

Figure 3.7: Prosys II resistivity management software.

The software also provides several additional processing functions and hence only the basic steps followed in this study for the processing of the acquired data sets are described and discussed.

Initially, the gap fillers of the measurement protocols used to reduce the number of injections, were removed, as well as possible outliers which may affect the data misfits (Fig.3.8). Afterwards, some basic parameters of the resistivity data were used to filter data, namely the apparent resistivity range, the data repeatability errors and the injection current (Fig.3.9).

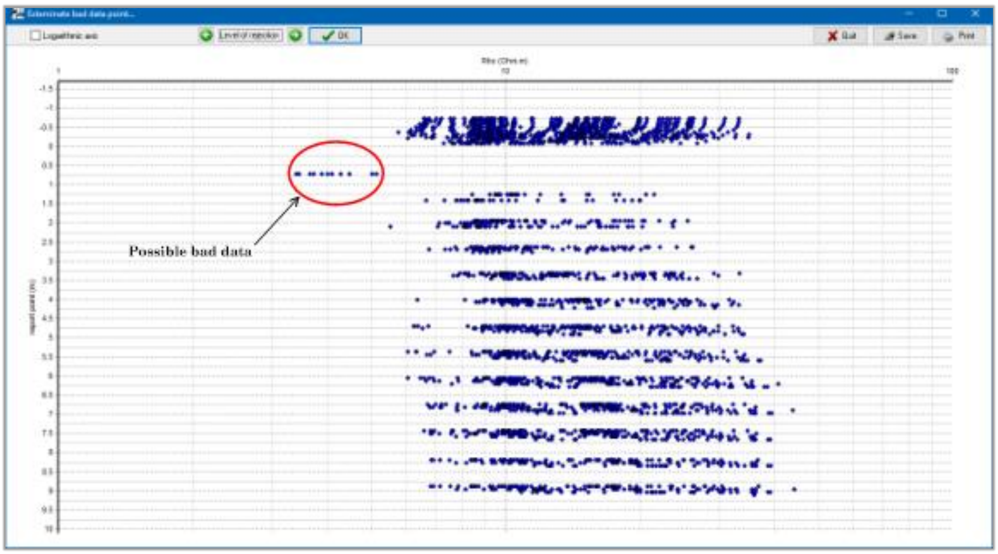

Figure 3.8: Distribution of resistivity data in Prosys II.

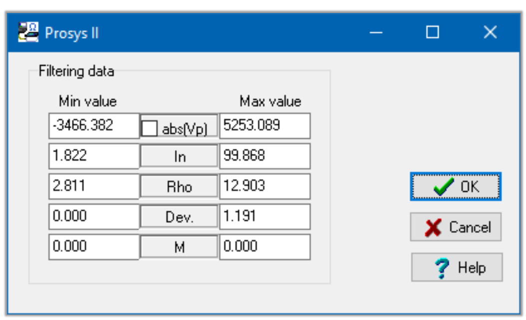

Figure 3.9: Filtering resistivity data, by Prosys II.

Despite the fact that Prosys II software can export the resistivity data to a range of output files, it cannot export cross-hole ERT data compatible with any inversion software. As mentioned before, the CrosProOpt protocol generator was also used to convert cross-hole binary files to files supported by the DC2DPRO and RES2DINV inversion software.

3.2.3 Inversion program (DC 2DPRO)

In this work, the DC2DPRO inversion software (Fig.3.10) was extensively used to perform the inversion of the collected ERT measurements, to obtain the real resistivity distribution of the subsurface structure. The steps that are usually followed for the inversion of the acquired ERT data sets through DC2DPRO inversion software and were followed in this study, are described below.

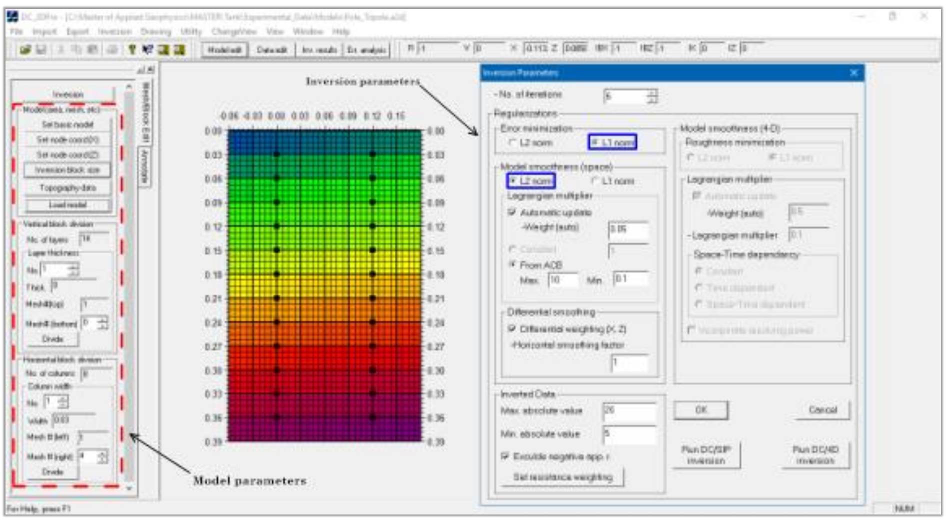

Figure 3.10: Description window of the main inversion and model parameters by the DC2D PRO software.

Initially, the data file that contains the measured apparent resistivity values and the information about the geometry of the measurements is inserted in the software. Following this step, the model parameterization, i.e. the number, division and size of model blocks for performing the 2-D inversion is decided either automatically or by the user on the basis of the measurement geometry.

The simultaneous minimization of the data misfits and the roughness of the model is controlled by the inversion parameters panel (Fig. 3.10). In this study, this minimization was realized by using minimization on the basis of either the L1 or L2 modes. Additional inversion parameters, including horizontal smoothing factor, Lagrangian multiplier etc. can be provided to the DC2DPRO inversion software.

Finally, the DC2DPRO inversion software allows also the visualization of the resistivity data and error analysis, and the editing of possible "bad" apparent resistivity values, as it is shown in Figure 3.11, while it supports various of output files for saving the inversion results.

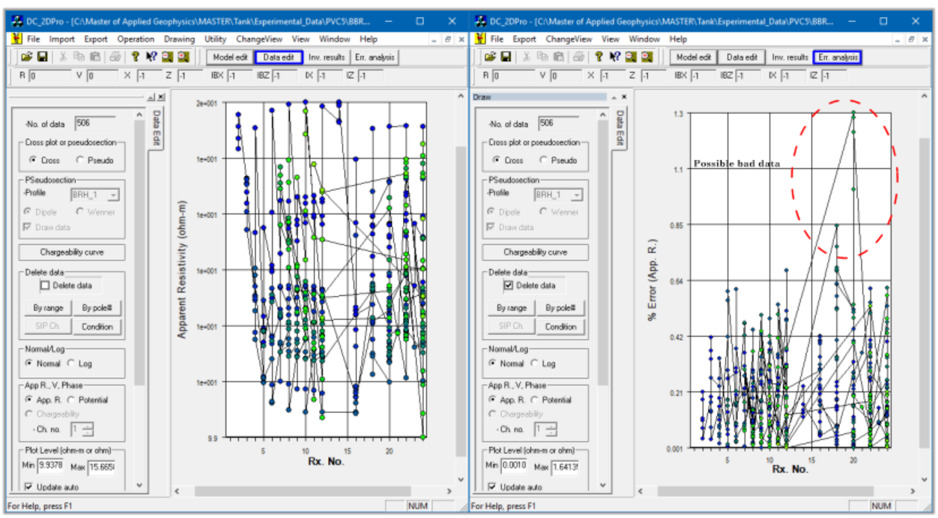

Figure 3.11: DC2D PRO data edit and error analysis windows.

CHAPTER 4

Experimental setup and inversion results

Chapter 4 provides the general design of the cross-hole ERT measurement experiments and their inversion results for different electrode array configurations, varying geoelectrical conditions and different PVC borehole casings.

More specifically, it presents and describes the setup of the experiments, including the modelling bodies of different resistivity, the tested borehole casings constructed for the simulation of different slot density and the examined electrode array configurations along with the results of the forward modelling of the examined experimental setup, in order to evaluate the response of each one to different resistivity distributions.

Finally, the inversion results of the experimental cross-hole ERT measurements for the different cases are presented and discussed. Moreover, the average apparent resistivity, for every electrode configuration, modelling body and borehole casing, is presented and commented.

4.1 Experimental design and setup

4.1.1 General setup

All the experiments were carried out, into a properly formed plastic tank with dimensions 125 cm (length) × 80 cm (width) × 90 cm (height) and an overall volume of 0.9 m^3, filled with tap water up to 60cm. The cross-hole ERT experiments comprise of 2 miniature multi-electrode cables, each with 12 embedded measuring copper electrodes, spaced at a 3 cm interval. For the simulation of the borehole-casings, three pairs of plastic PVC-tubes of different slot density were constructed and used. Also, special bases were constructed to restrain the cables to specific depth level, support and stabilize the PVC-tubes. The general setup of the experiments is presented in Fig.4.1.

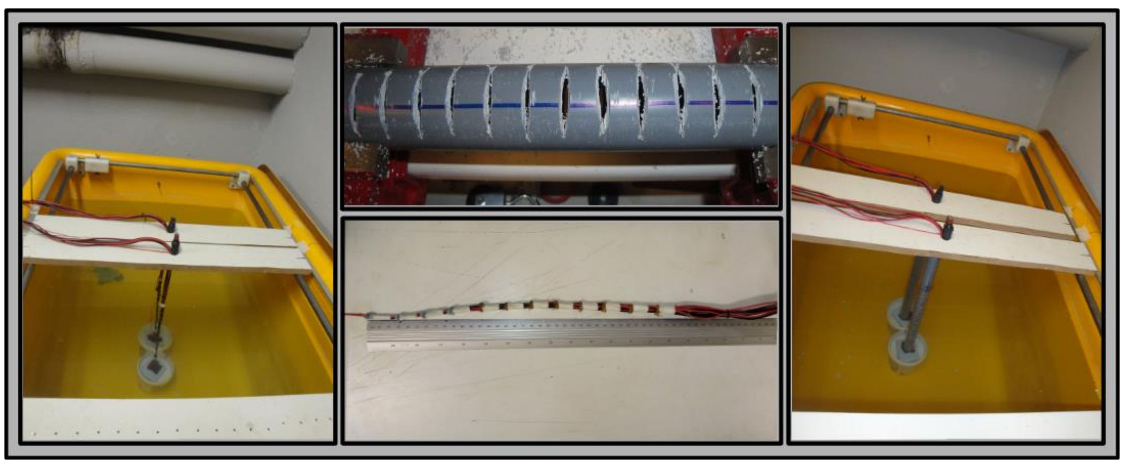

Figure 4.1: Setup of the experiments.

The upper electrode of each cable was sunk 3 cm under the water table, while the deepest electrode was located at a distance of 12 cm above the support bases of the borehole-casings. In the case of pole-dipole array, the remote current electrode was placed on the surface, between boreholes, at an equal distance from both.

4.1.2 Modelling environments

Three experimental modelling environments setups have been created for the cross-hole ERT measurements ranging from a homogeneous background, to various resistive and conductive targets.

The first environment setup represents a homogeneous medium of water with average conductivity of 600 μS/cm (i.e. 15 Ohm-m, Fig.4.2). The second environment setup involves the presence of a conductive ore body between the boreholes (Fig.4.3) and the third environment setup involves the presence of a resistive body (Fig.4.4).

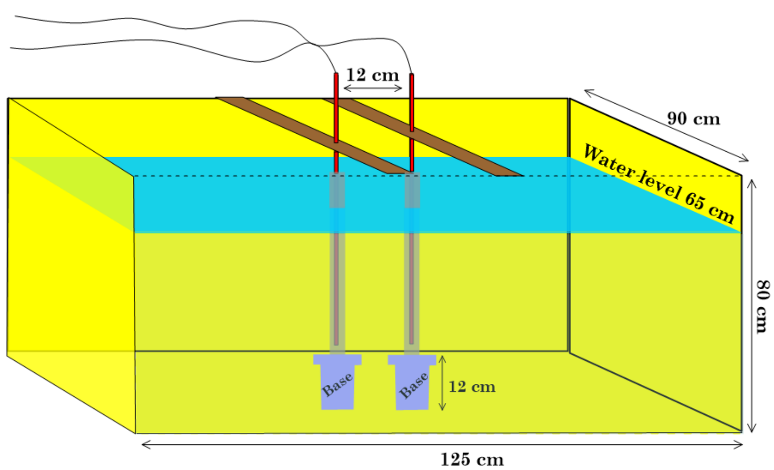

Figure 4.2: 3D Illustration of the first homogeneous experimental environment setup.

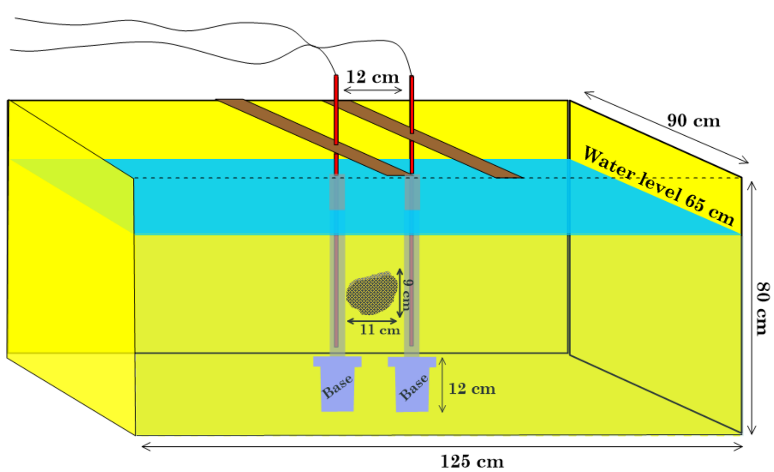

Figure 4.3: 3D Illustration of the second experimental environment setup, with a conductive target.

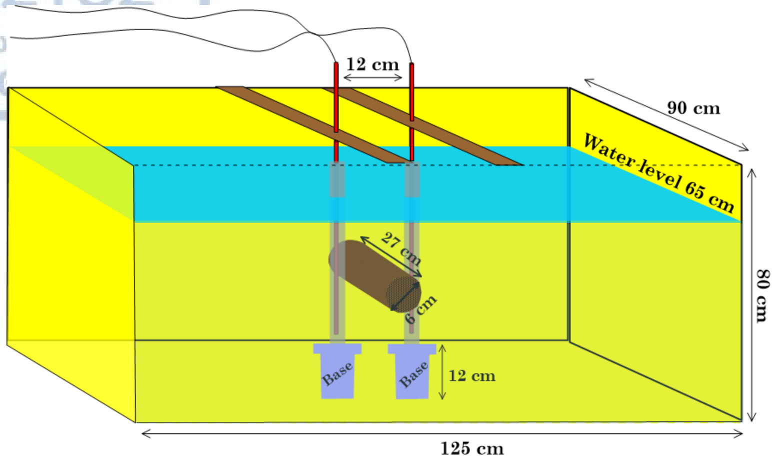

Figure 4.4: 3D Illustration of the third experimental environment setup, with a resistive target.

4.1.3 Modelling targets

The targets used for setting up the second and third experimental inhomogeneous environments setups were a piece of iron pyrite and a plastic bottle, respectively. The expected 2D shape of the resistive target was circular, with 6-7 cm diameter (Fig.4.5 a, b), while the conductive target had approximate dimensions 10 cm (length) × 9 cm (width) (Fig.4.5 c, d). The conductive target was located between 6st and 9st electrode, while, the resistive target was placed between 6st and 8st electrode. Both targets were sunk 19 cm below the water surface.

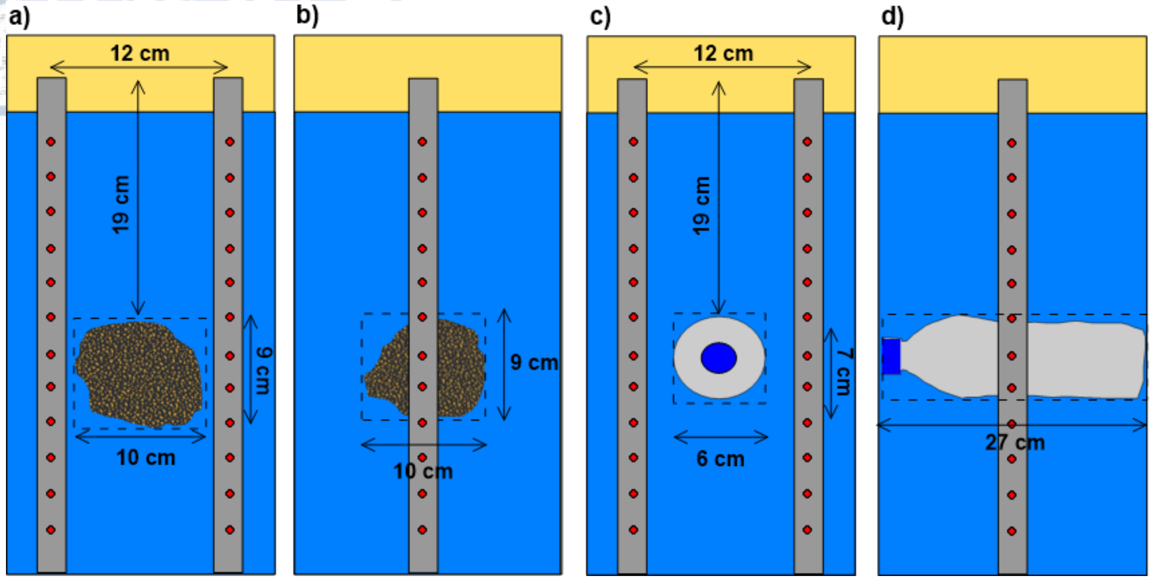

Figure 4.5: Front and side view of the conductive (a, b) and resistive (c, d) target, respectively.

4.1.4 Borehole-casings

For the simulation of the borehole-casings three pairs of plastic PVC-tubes of 3.2 cm diameter were constructed, each one with a different slot density (Fig.4.6). Borehole-casing no.1 has the smallest density of slots (2 slots per electrode spacing), borehole casing no.2 had 4 slots per electrode spacing and borehole-casing no.3 had the largest density of slots (6 slots per electrode spacing). The main attributes of each pair of the borehole-casings, are shown in Table 1.

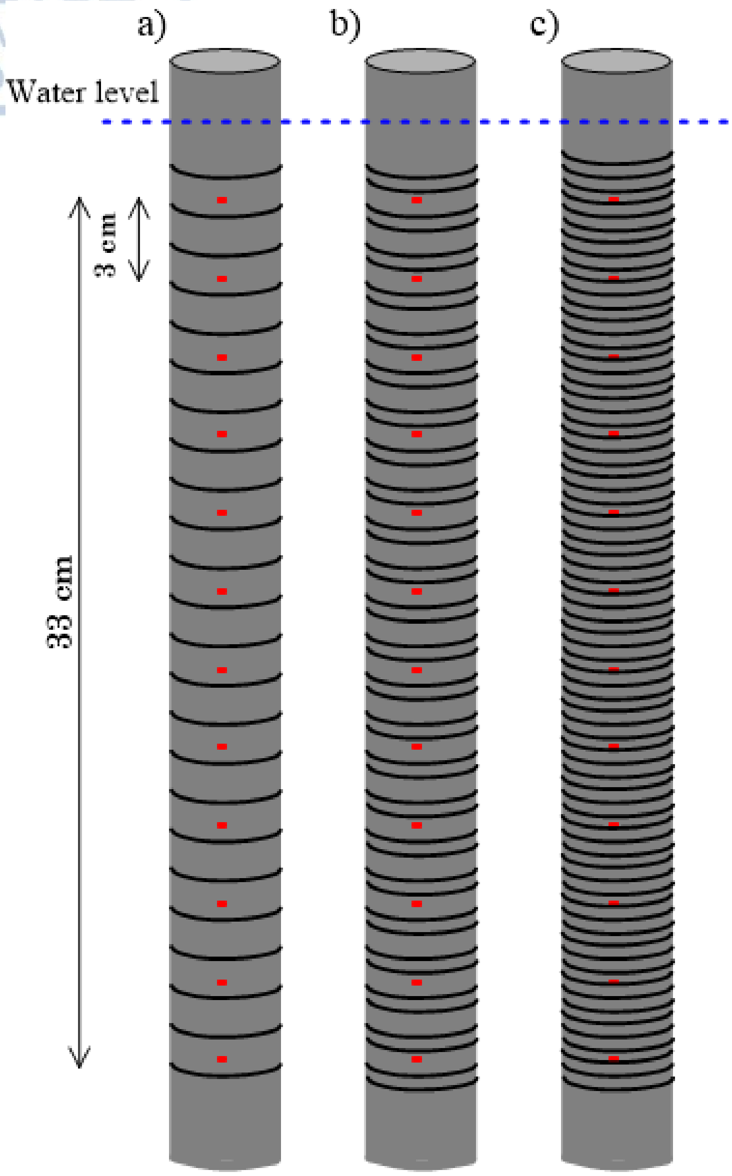

Figure 4.6: Schematic presentation of the borehole-casing, along with the electrodes (red circles) and the slots (elliptical symbols): a) borehole-casing no.1, b) borehole-casing no.2, c) borehole-casing no.3.

No. Borehole-casing	Number of slots (overall)	Spacing of slots(cm)	Slots/ Electrode
1	24	1.5	2
2	48	0.75	4
3	96	0.50	6

Table 1: Attributes of the different borehole-casings.

4.1.5 Electrode arrays

The tested protocols (generated by the CrosProOpt module) that were used for obtaining the experimental datasets involved the bipole-bipole, pole-dipole and pole-tripole electrode configurations. The way the electrode configurations were realized within each protocol is explained in this section. In order to represent the electrode array configurations, the current and potential electrodes are symbolized as, CA, CB and PM, PN, respectively, the basic inter-electrode spacing along the z (depth) axis is symbolized as D and the separation between measuring electrodes is expressed an integer multiple "n" of the basic spacing D.

Bipole-Bipole array

There are three different independent electrode configurations for bipole-bipole array for the realization of cross-hole ERT measurements (Bing and Greenhalgh, 2000), CAPM-CBPN, CAPM-PNCB, CACB-PMPN. The bipole-bipole electrode configurations, where the current and potential electrodes are positioned in different boreholes (i.e. CAPM-CBPN and CAPM-PNCB), produce similar imaging results, which are of good quality, while the signal to noise ratio is high (Leontarakis and Apostolopoulos, 2012, 2013). One additional advantage of the bipole-bipole array is the low sensitivity to the electrode displacement (Simyrdanis et al., 2013). On the other hand, it has been shown that the configuration involving the positioning of the two dipoles (current and potential) into different boreholes (CACB-PMPN) exhibits low quality signal (i.e. small observed potential differences) so generally this configuration is not preferable.

In this work, only the C_AP_M-C_BP_N bipole-bipole electrode configuration is used for the realization of the cross-hole ERT measurements, with the placement of the dipoles C_AP_M and C_BP_N into different boreholes (Fig.4.7). The source electrodes C_A-C_B are always positioned at the same depth level. For every current electrode pair location all combinations of potential differences among the electrodes positioned above the sources are recorded. Consequently, the current electrodes are moved one electrode step upwards and the potential difference collection procedure is repeated.

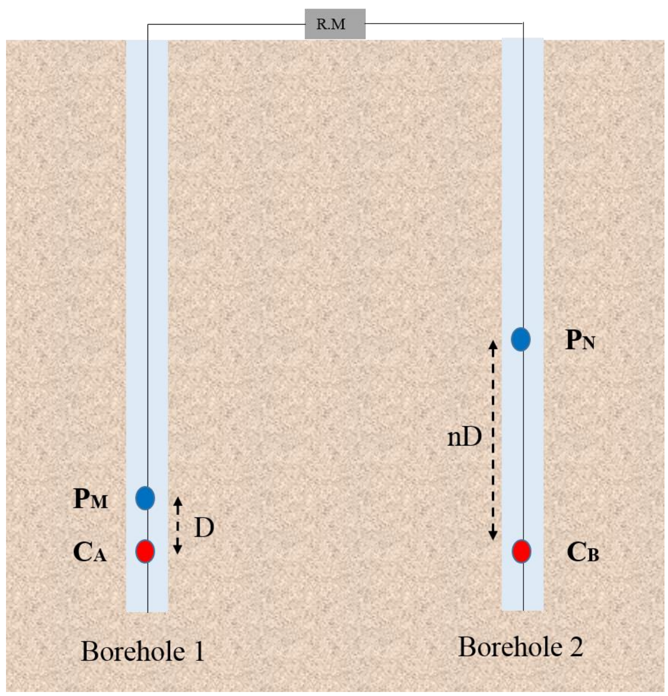

Figure 4.7: Bipole-bipole C_AP_M-C_BP_N electrode and protocol configuration.

Part of the protocol of the bipole-bipole electrodes sequence for two 24-electrodes boreholes is shown in Fig.4.8 (left). The sensitivity analysis of a particular data point (no 19) is presented in Fig.4.8(right) using a rainbow scale with cold (blue) and hot (red) colors indicating negative and positive sensitivity values respectively while green-yellow colors representing very low (near zero) sensitivity. The resulting sensitivity distribution indicates that the area between the boreholes appears high positive values, while the areas between the current and potential electrodes at each borehole, by contrast, present large negative values.

#	C1	C2	P1	P2
1	1	48	2	47
2	1	48	2	46
3	1	48	2	45
4	1	48	2	44
5	1	48	2	43
6	1	48	2	42
7	1	48	2	41
8	1	48	2	40
9	1	48	2	39
10	1	48	2	38
11	1	48	2	37
12	1	48	3	47
13	1	48	3	46
14	1	48	3	45
15	1	48	3	44
16	1	48	3	43
17	1	48	3	42
18	1	48	3	41
19	1	48	3	40
20	1	48	3	39
21	1	48	3	38
22	1	48	3	37

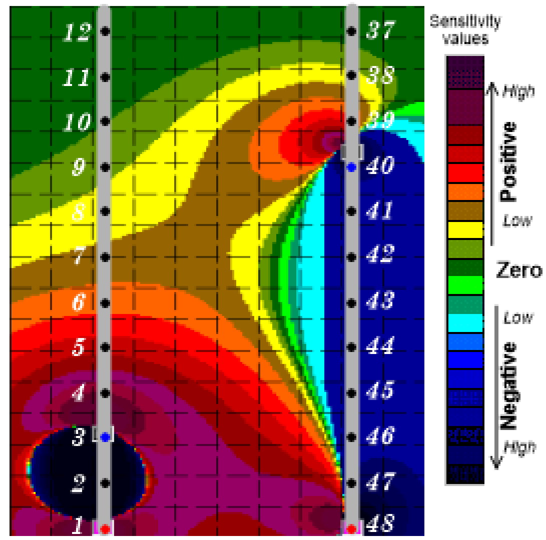

Figure 4.8: Sensitivity distribution (right) of a random measurement (left-red frame) of bipole-bipole array.

Pole-Dipole array

Several authors recommend this electrodes configuration due to its efficient resolution and target detection (Leontarakis and Apostolopoulos, 2012, 2013). Although pole-dipole array presents various independent configurations, for this work and specifically for the enhancement of the spatial resolution of the cross-hole ERT measurements, the CA-PMPN and PMPN-CA arrangements were used.

More specifically, in this array (Fig. 4.9) the injection electrode CA and the potential dipole PMPN are always located into different boreholes, while the location of the remaining injection electrode CB is fixed on the surface (depth=0m) between boreholes, usually at an equal distance from both boreholes, far from the CA, PM and PN electrodes. The current electrode CA is moving with a step equal to the basic inter-electrode spacing, while, the dipole PMPN moves along the other borehole with all possible separations.

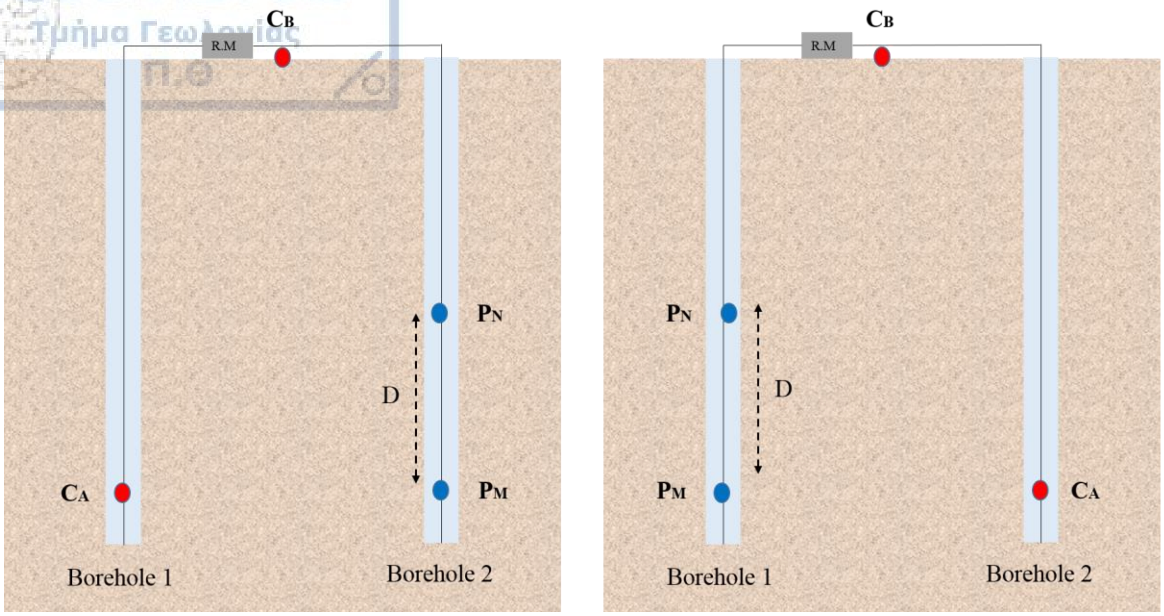

Figure 4.9: Pole-dipole C_A-P_MP_N (left) and dipole pole P_MP_N-C_A (right) electrodes configurations.

The large positive (red color) sensitivity values are focused in the zones of potential and current dipoles, covering significant parts between the boreholes and providing information for the area of interest, while large negative (blue color) sensitivity can be observed between C_A-P_M and C_B-P_N (Fig. 4.10).

#	C1	C2	P1	P2
1	1	25	48	47
2	1	25	48	46
3	1	25	48	45
4	1	25	48	44
5	1	25	48	43
6	1	25	48	42
7	1	25	48	41
8	1	25	48	40
9	1	25	48	39
10	1	25	48	38
11	1	25	48	37
12	1	25	47	46
13	1	25	47	45
14	1	25	47	44
15	1	25	47	43
16	1	25	47	42
17	1	25	47	41
18	1	25	47	40
19	1	25	47	39
20	1	25	47	38
21	1	25	47	37
22	1	25	46	45

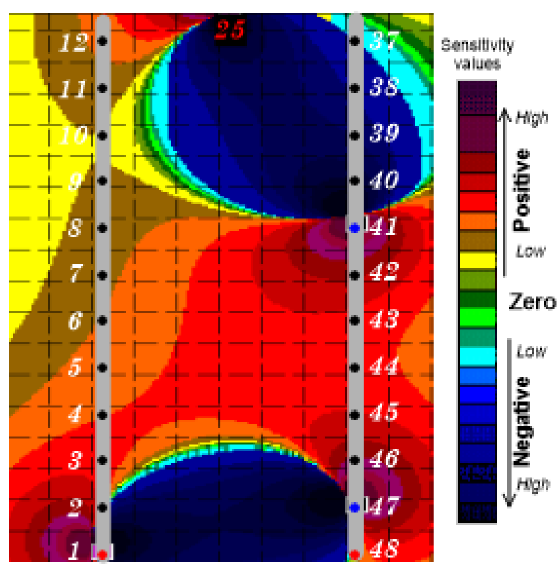

Figure 4.10: Sensitivity distribution (right) of a random measurement (left-red frame) of pole-bipole protocol.

Pole-Tripole array

Goes and Meekes (2004) where the first to propose the pole-tripole electrode array configuration for the realization of cross-hole ERT measurements. Although, pole-tripole array presents various independent configurations, in this work the examined pole-tripole array corresponds to the $C_AP_MP_N$-C_B and C_B-$C_AP_MP_N$ configurations. In this array, the current electrode C_B is located in one borehole and the remaining three electrodes, C_A, P_M and P_N, are placed in the other borehole (Fig.4.11). As can be seen in Figure 4.11 the tripole $C_AP_MP_N$ moves upwards and then becomes $P_NP_MC_A$ and moves downwards for all the separation factor values, n, between the injection pole C_A and the potential dipole (P_MP_N). When this sequence is completed, and a full sub-set has been collected for the tripole, the current electrode C_B (at the other borehole) moves one electrode step upwards and a new tripole sub-set is obtained. When the full data set is collected for the $C_AP_MP_N$-C_B configuration, the procedure is repeated similarly for the C_B-$C_AP_MP_N$ configuration.

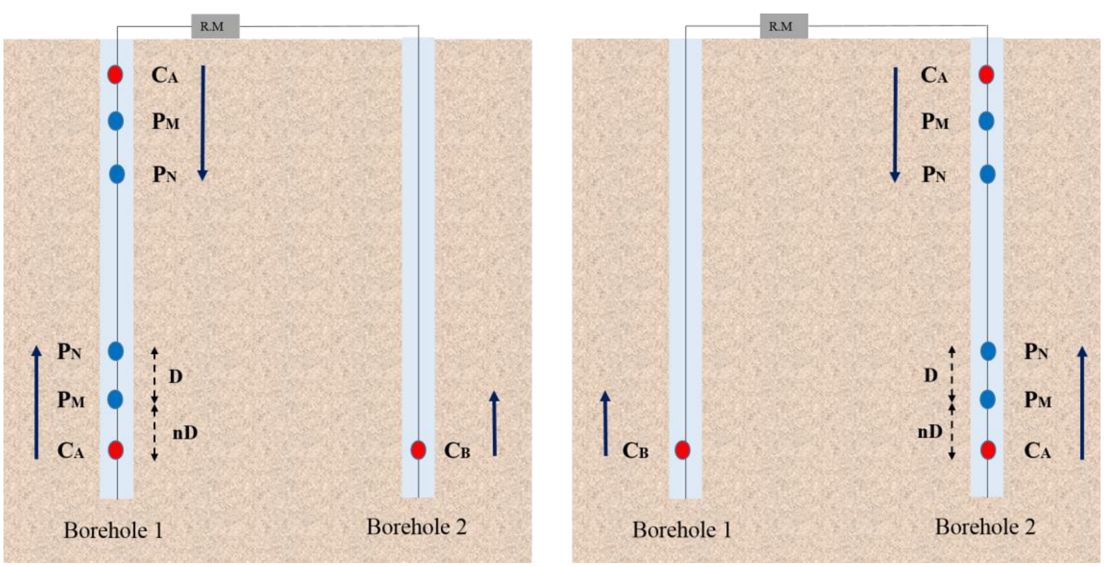

Figure 4.11: Pole-tripole C_B-$C_AP_MP_N$ (left) and tripole-pole $C_AP_MP_N$-C_B (right) electrode configurations.

In figure 4.12, the sensitivity distribution of the pole-tripole array indicates that high positive sensitivity values (red color) appear in the area between the potential electrodes and also between the injection electrode CB and potential dipole. The rest of the area presents either large negative (blue color) or very low (green/yellow color) positive sensitivity values.

#	C1	C2	P1	P2
1	48	1	47	46
2	48	1	46	45
3	48	1	45	44
4	48	1	44	43
5	48	1	43	42
6	48	1	42	41
7	48	1	41	40
8	48	1	40	39
9	48	1	39	38
10	48	1	38	37
11	47	1	46	45
12	47	1	45	44
13	47	1	44	43
14	47	1	43	42
15	47	1	42	41
16	47	1	41	40
17	47	1	40	39
18	47	1	39	38
19	47	1	38	37
20	46	1	45	44
21	46	1	44	43
22	46	1	43	42

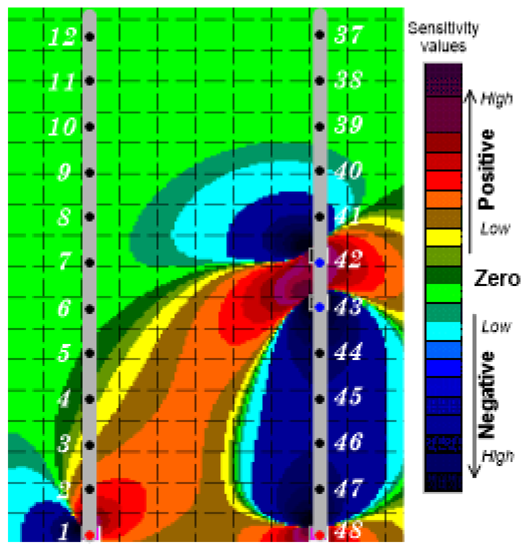

Figure 4.12: Sensitivity distribution (right) of a random measurement (left-red frame) of pole-tripole protocol.

4.2 Cross-hole ERT measurements for synthetic models

Before using the measuring protocols into the tank environment, we produced synthetic data using numerical modeling for different resistivity models. This allowed us to obtain a first estimate of the effectiveness of each protocol, for the different resistivity distributions, without the effect of the presence of the borehole-casings.

The general setup of the cross-hole geometry is equivalent to the one used for the experimental data collection i.e. the distance between the boreholes is 12 cm, while at each borehole there are 12 electrodes, spaced at a 3 cm interval. Model 1 is just a homogeneous medium of 10 ohm-m resistivity (Fig.4.13a), model 2 involves a 3x3 cm conductive prism of 1 ohm-m resistivity (Fig.4.13b) and model 3 involves a 100 Ohm-m resistive 3x3cm prism as a target (Fig.4.13c). No noise is included to the synthetic resistivity model.

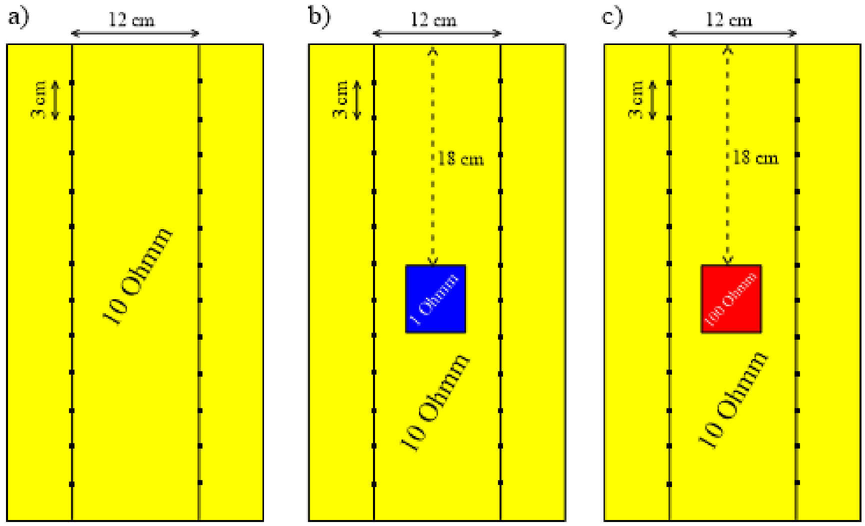

Figure 4.13: Synthetic resistivity models. a) Homogeneous medium, b) Conductive target and c) Resistive target.

The inverted results of every row and column in Fig.4.14, correspond to a different electrode array configuration and to a different synthetic resistivity model, respectively. All geoelectrical images are presented on a logarithmic rainbow scale, with the blue color corresponding to low resistivity values and the red color to high resistivity values. The black border indicates the size and position of the targets.

In general Fig.4.14 shows that all electrode array configurations produce good quality results for all tested models. However, the inversion results of the bipole-bipole array (Fig. 4.14 a-c) seem to be better, producing limited artefacts, compared to the other electrode arrays.

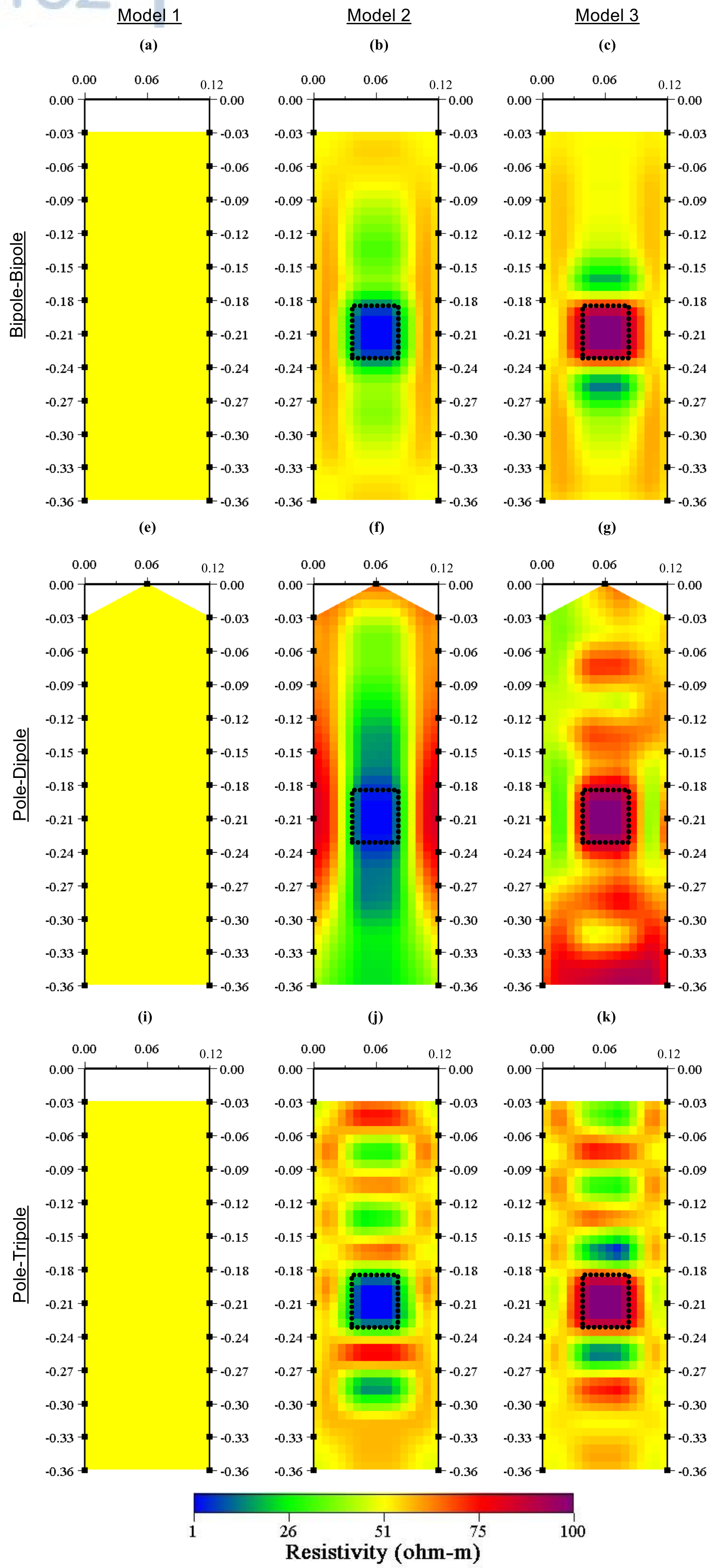

Figure 4.14: Results of the numerical modelling for the different resistivity models and different electrode arrays.

More specifically, in the case of the homogeneous background, all electrode arrays (Fig. 4.14 a, e, i) performed well, showing the expected resistivity distribution. Under the presence of the target, either conductive or resistive, both pole-tripole (Fig. 4.14 f, g) and mainly pole-dipole (Fig. 4.14 j, k) measurement protocols present some artefacts along the electrode line even though both reconstruct the targets quite satisfactorily.

4.3 Experimental cross-hole ERT inversion results

In this section, the 2D experimental cross-hole ERT inverted results for the different modelling environments, different borehole-casings and different electrode configurations, are presented.

In general, 36 full cross-hole ERT datasets were obtained, involving the combination of three (3) different protocols (i.e. three different electrode arrays) previously described, four (4) borehole-casing configurations (3 slotted ones and a reference one, with no casing) and three (3) modelling environment setups (Fig.4.15).

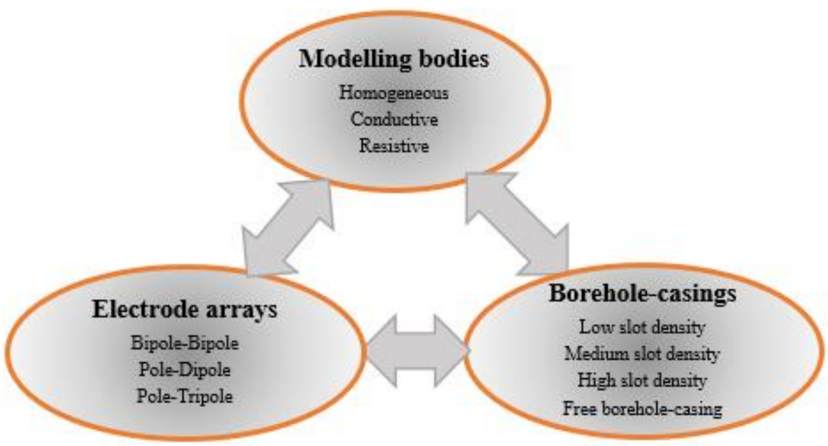

Figure 4.15: Schematic diagram of the experimental tests performed.

Table 2, presents the total number of the data of the measurement protocols for the different electrode array configurations, as they were used for the realization of the experimental cross-hole ERT measurements.

Array	No. of data/protocol
Bipole-Bipole	506
Pole-Dipole	1564
Pole-Tripole	1514

Table 2: Number of data measured for each array.

The results of every row correspond to a different electrode array protocol, namely the bipole-bipole, pole-dipole and pole-tripole arrays, respectively. The first three columns of every figure correspond to a different borehole-casing (no1, no2 and no3, respectively as shown in Figure 4.6), while the images of the last column show the inversion results for the case of no borehole, corresponding to a casing-free response of the resistivity distribution. Furthermore, for each experimental environment, special graphs of the apparent resistivity distribution of every dataset along with its average are shown in the corresponding results, presenting the variation of the apparent resistivity distribution due to the different borehole-casings.

The final results were obtained after 6 iterations, reaching an average RMS error below 1% between the measured and predicted data for all the datasets. The inverted geoelectrical images are presented with a logarithmic rainbow scale, where the blue colors correspond to low resistivity values, while the red colors correspond to high resistivity values.

4.3.1 Homogeneous background

The inversion results presented in Fig. 4.16 for the case of a homogeneous background show that bipole-bipole and pole-tripole arrays suffer from the presence of PVC cased boreholes, leading to low quality results. On the other hand, the pole-dipole array results in the optimal images, as it presents with accuracy and limited artefacts the resistivity distribution of the homogeneous background, approaching the ideal condition of the case of no borehole-casing.

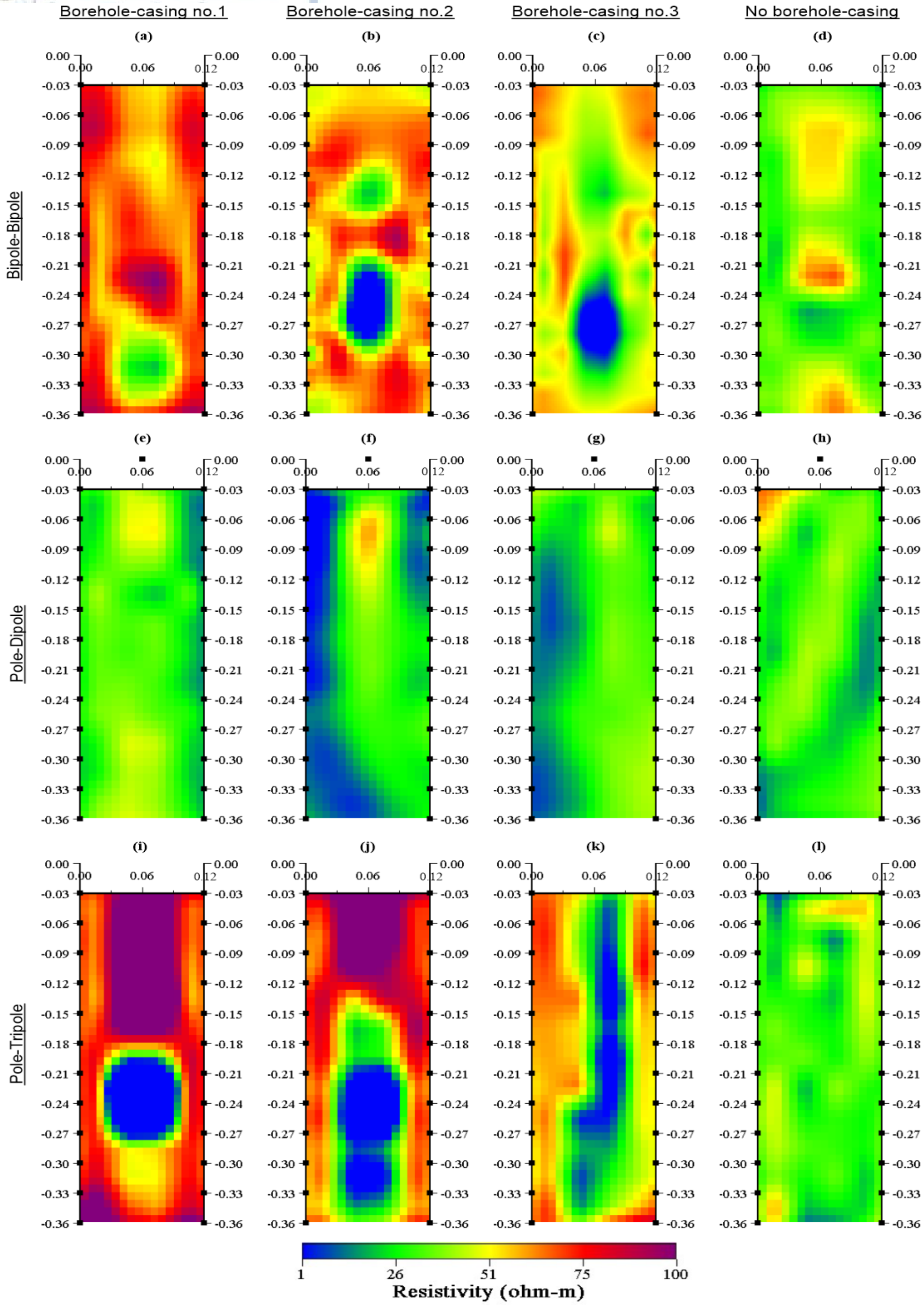

Figure 4.16: Inversion results for homogeneous environment for different measurement arrays and borehole casing.

Using the borehole-casing no.1 (the one with the fewer number of slots), bipole-bipole array (Fig.4.16a) exhibits a resistive artefact in the middle of the section between boreholes, while in the surrounding area the resistivity distribution ranged between 2 Ohm-m and 10 Ohm-m. Along the electrodes in both sides of the resistive artefact, high resistivity values also appear due to the borehole-casings. A small artefact also appears in the second electrode of the left borehole. It is obvious that pole-tripole array (Fig.4.16i) exhibits the worst inversion results, since the only reliable information concerns a small area between boreholes, where the resistivity ranges within expected values. The imaging of the upper part of the section between the boreholes is totally unrealistic presenting very large resistivity values. The inversion results of pole-dipole array (Fig.4.16e) present an almost uniform resistivity value in the whole section and only limited resistive artefacts can be seen.

Although, under the presence of borehole-casing no.2, both bipole-bipole and pole-tripole arrays produce better results than in the case of borehole-casing no.1, still large resistivity values distort the images, especially for the pole-tripole array. Specifically, the bipole-bipole array (Fig.4.16b) shows the same resistive artefacts in the middle of the section, as in the case of borehole-casing no.1, but to a lesserextent. The pole-tripole array (Fig.4.16j) still suffers from high resistivity values, even though they are reduced comparatively to the previous borehole-casing. Once again, the inversion results of pole-dipole array are optimal in reconstructing the homogeneous background realistically, with no notable artefacts (Fig.4.16f).

In the last borehole-casing no.3 (with the largest slot density), the results of bipole-bipole and pole-tripole arrays are clearly improved, producing images of better quality than in the previous borehole-casings no.1 and no.2, respectively. Although, both present constant resistivity distribution in the area between the boreholes, unrealistic resistive anomalies indicate the effect of the borehole-casings (Fig.4.16c&k). the pole-dipole array (Fig.4.16g) presents almost the same resistivity distribution, as in borehole-casings no.1 and no.2, with no sign of artefacts.

Fig.4.17 presents the measured apparent resistivity values with respect to the number of the data points and the average apparent resistivity, for every electrodes configuration and borehole-casing. In the case of no borehole-casing (blue color), the average of apparent resistivity for all the electrode configurations varies beteween7-8 Ohm-m.

As expected, the average apparent resistivity, for both bipole bipole and pole tripole, is quite high (26-27 Ohm-m), when the borehole-casing no.1 is used, while gradually, as the density of borehole slots increases, the apparent resistivity values decrease, lowering also the average apparent resistivity. On the other hand, pole-dipole array presents systematically lower apparent resistivity values, exhibiting almost the same average apparent resistivity for all casings (i.e. 7-8 Ohm-m). Note that the reduction trend of the average apparent resistivity with different casings, observed for the bipole-bipole and pole-tripole arrays, is also observed for this array, though to a very limited extent.

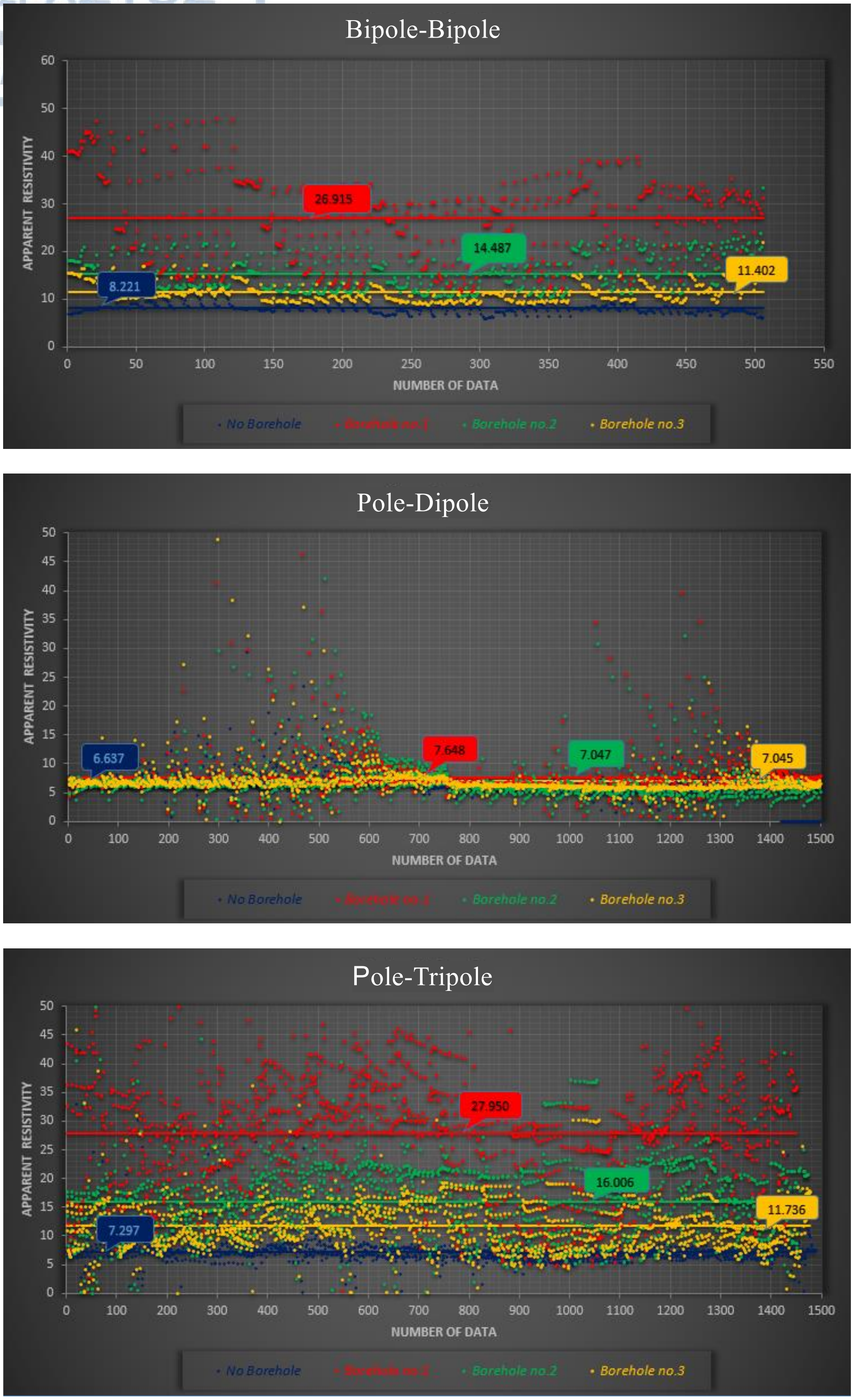

Figure 4.17: Plots of apparent resistivity values and averages (colored lines and frames) apparent resistivity, relative the number of the data points for each array and borehole casing (blue color-no borehole, red color-borehole casing no.1, green color-borehole-casing no.2 and yellow color-borehole-casing no.3).

4.3.2 Conductive target

In the presence of a conductive target in the middle part of the section between boreholes, all electrode arrays show significant resistive artefacts, disturbing the resistivity distribution of the subsurface structure (Fig.4.18). However, the pole-dipole array produces better images compared to the bipole-bipole and pole-tripole arrays, despite the fact that the low resistivity contrast between target and background makes the distinction of the conductive target more difficult.

In the presence of borehole-casing no.1, both bipole-bipole and pole-tripole arrays present very poor quality images. Specifically, the bipole-bipole array (Fig.4.18a) results are particularly distorted and exhibit significant resistive artefacts, especially in the area between the boreholes where the conductive target should have been imaged. The inverted resistivity distribution ranges between 1 Ohm-m to 100 Ohm-m. The pole-tripole array (Fig.4.18i) presents exactly the same image as in the case of the homogeneous background and hence, the inversion results of this cannot be considered as being reliable, despite the presence of the conductive body. Lastly, the pole-dipole array (Fig.4.18e), despite some resistive artefacts, reconstructs the conductive target and the overall results in a a much better way than the other 2 arrays.

Using borehole-casing no.2, bipole-bipole and pole-tripole arrays show an improvement in their inversion results, but still, both (mainly the pole-tripole) are unable to reconstruct properly the conductive target. The pole-dipole array results depict the conductive target satisfactorily, however still a resistive artefact at the upper part of the section is present (Fig.4.18f).

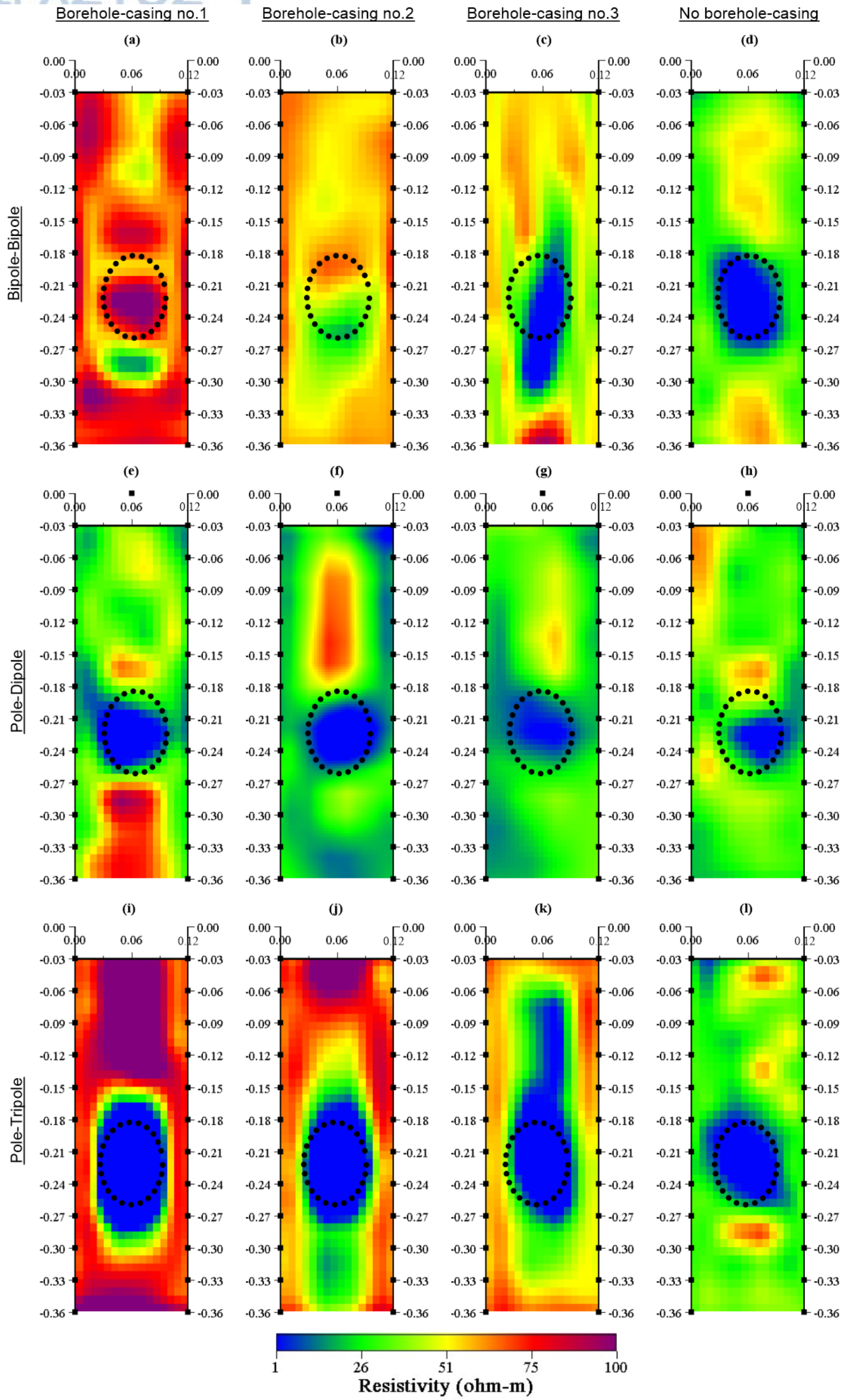

Figure 4.18: Inversion results under the presence of a conductive target for different measurement arrays and borehole casing.

Under the presence of the borehole casing with a higher density of slots (borehole-casing no.3), both bipole-bipole and pole-tripole arrays produce improved images and seem to be able to reconstruct the resistive target while resistive artefacts are significantly fewer (Fig.4.18c&k). The pole-dipole array (Fig.4.18g) still presents the optimal images of all the arrays, but, unexpectedly, the conductive target is not so easily identified, probably due to the low contrast between target and background.

Overall, the pole-dipole array recovers the most efficient and reliable inverted images, for the different borehole-casings, approaching almost the no borehole-casing response. The low contrast between conductive target and homogeneous background and the presence of the borehole-casings, do not allow the bipole-bipole and pole-tripole arrays either to properly image the resistivity distribution of the subsurface, or to illustrate the conductive target.

Figure 4.19 shows that the average apparent resistivity using the no borehole-casing (blue color) ranges between 6 and 7 Ohm-m for all the electrode configurations. The datasets of the bipole-bipole and pole-tripole arrays suffer from the presence of the borehole-casings, presenting high average apparent resistivity. On the contrary, the average apparent resistivity of the pole-dipole array for all the borehole casings, approaches to the value of the no borehole-casing response.

Moreover, as the number of borehole slots increases, all the arrays present either a large reduction of the apparent resistivity values, i.e. the bipole-bipole and pole-tripole arrays, or low reduction, i.e. pole-dipole array.

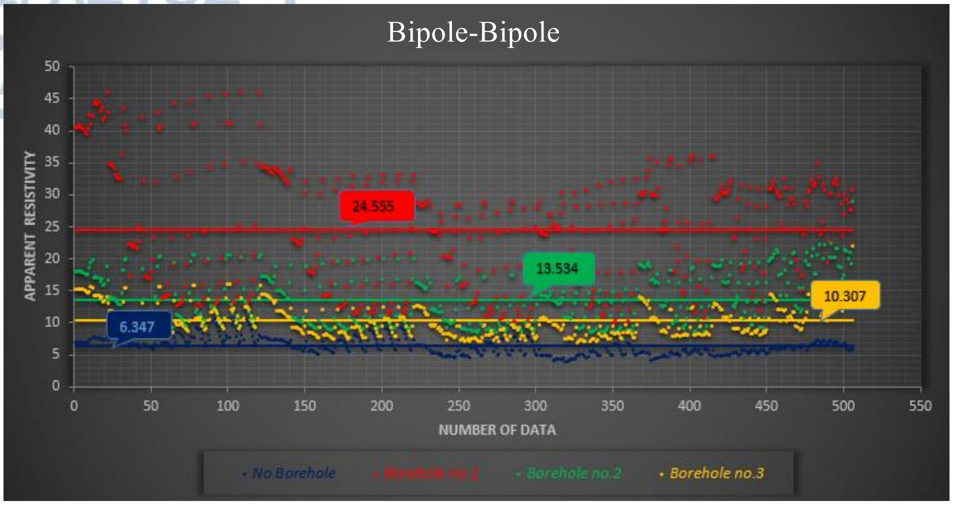

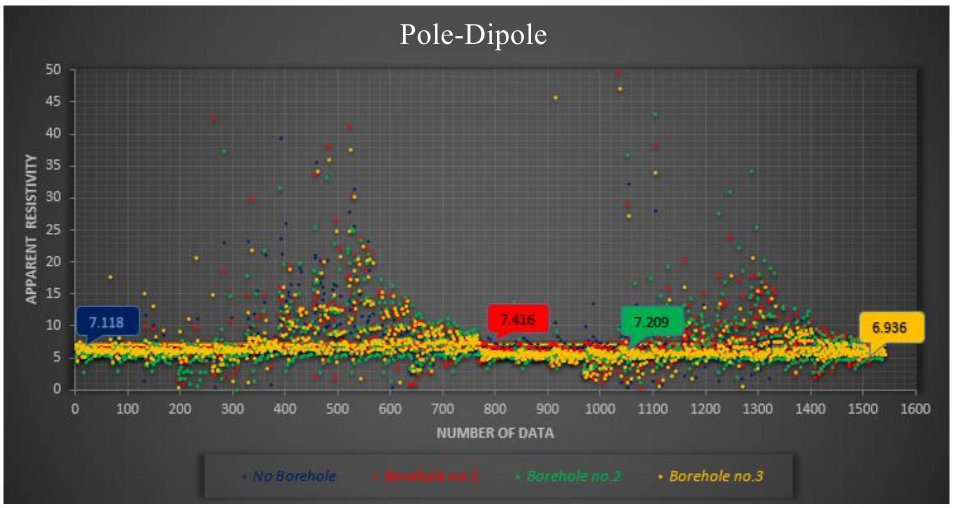

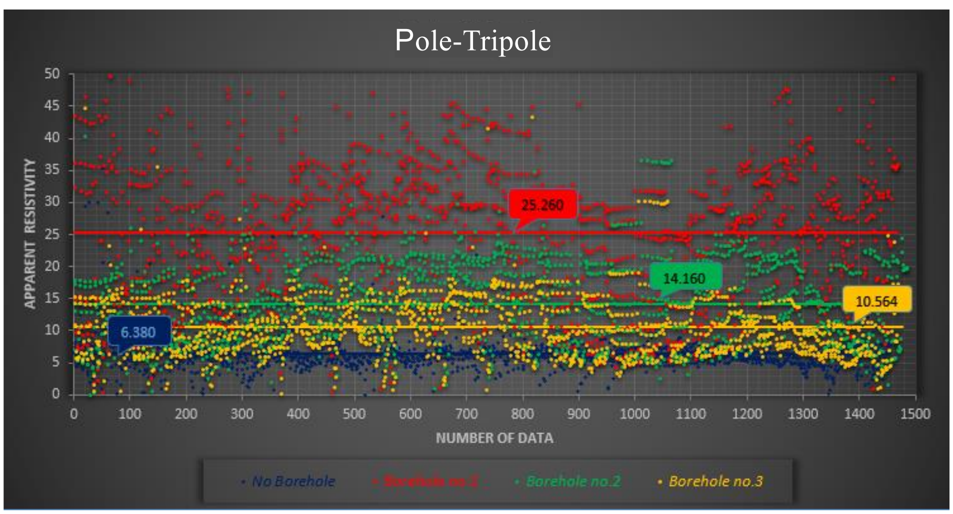

Figure 4.19: Plots of apparent resistivity values and averages (colored lines and frames) apparent resistivity, relative the number of the data points for each array and borehole casing (blue color-no borehole, red color-borehole casing no.1, green color-borehole-casing no.2 and yellow color-borehole-casing no.3).

4.3.3 Resistive target

As expected, the pole-dipole array produces the optimal images of all the arrays, reconstructing precisely the resistive target within the homogeneous medium, regardless of the density of borehole slots, as shown in Fig.4.20. Unlike the pole-dipole array, under the presence of borehole-casings, the bipole-bipole and mainly the pole-tripole array produce images of very poor quality, with severe resistive artefacts, even though, as the number of borehole slots increases, these artefacts are reduced, though to a limited extent.

In the presence of borehole-casing no.1, the pole-tripole array (Fig.4.20i) produces images of very poor quality, with highly resistive anomalies, as well as, serious resistive artefacts. Likewise, the bipole-bipole array (Fig.4.20a) exhibits highly resistive artefacts especially at the middle of the section as in the case of the conductive target. Both arrays cannot reconstruct a resistivity distribution similar to the no borehole-casing response. On the other hand, the pole-dipole array reconstructs the resistive target particularly well with very limited artefacts (Fig.4.20e).

The increase of the slot density of the borehole (borehole-casing no.2) still does not improve significantly the results for the bipole-bipole (Fig.4.20b) and the pole-tripole (Fig.4.20j) arrays as the resistive target either is still absent (pole-tripole) or barely identifiable (bipole-bipole). Conversely, the pole-dipole array (Fig.4.20f) produces a very good inversion images, with no significant artefacts.

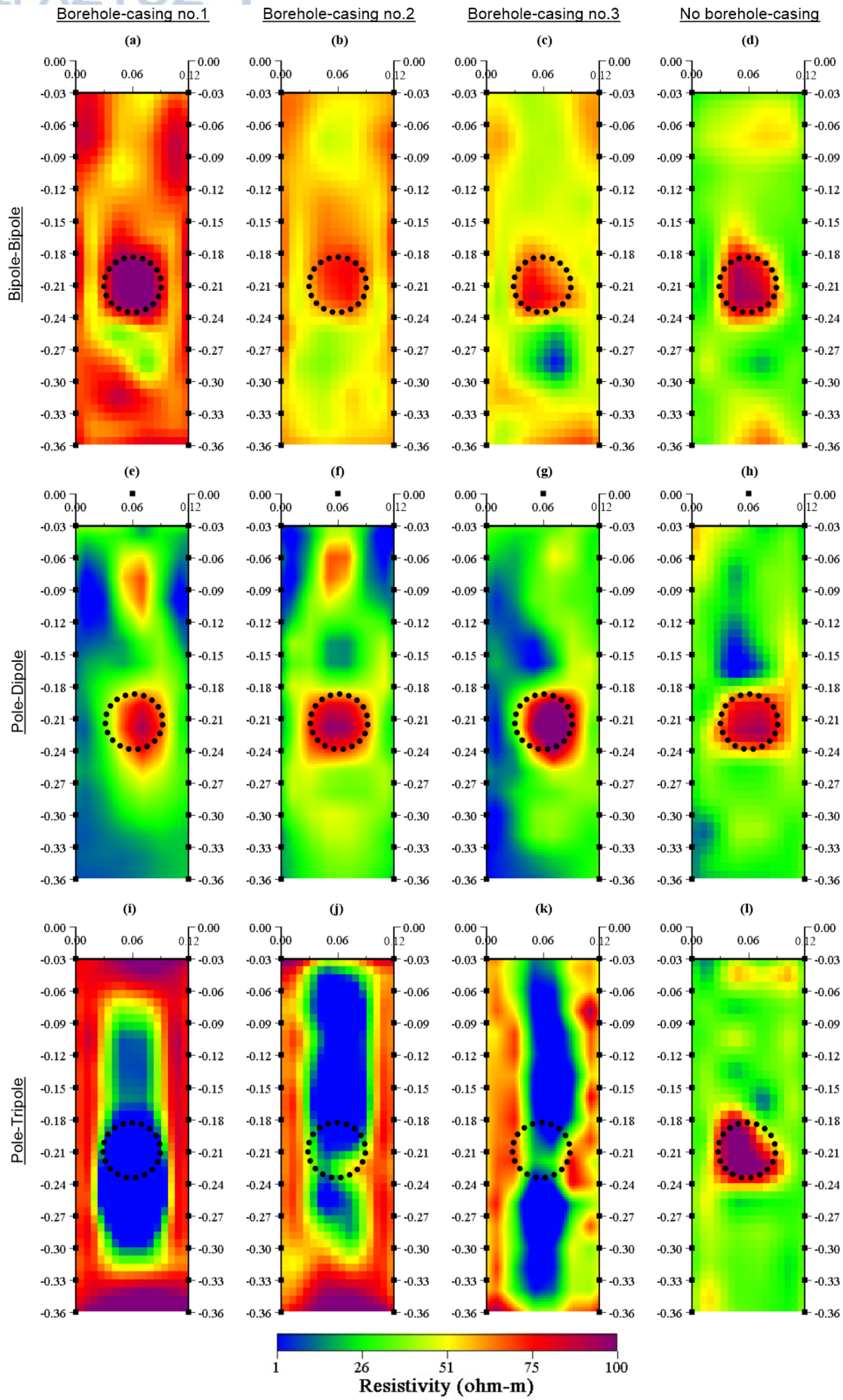

Figure 4.20: Inversion results under the presence of a resistive target for the measurement arrays and borehole casing.

Even in the case of the borehole-casing no.3, only the pole-dipole array (Fig.4.20g) is able to produce a good resistivity distribution, which is very similar to the no borehole-casing response. Pole-tripole (Fig.4.20l) still produces major resistive or conductive artefacts while the bipole-bipole array (Fig.4.20d) identifies somehow the resistive body but it is very difficult to be clearly distinguishable.

Fig.4.21 indicates that the average apparent resistivity for both bipole-bipole and pole-tripole data sets are extremely high, in the presence of the borehole-casing no.1. However, it is also observed that the average apparent resistivity, decreases as the density of the borehole slots increases.

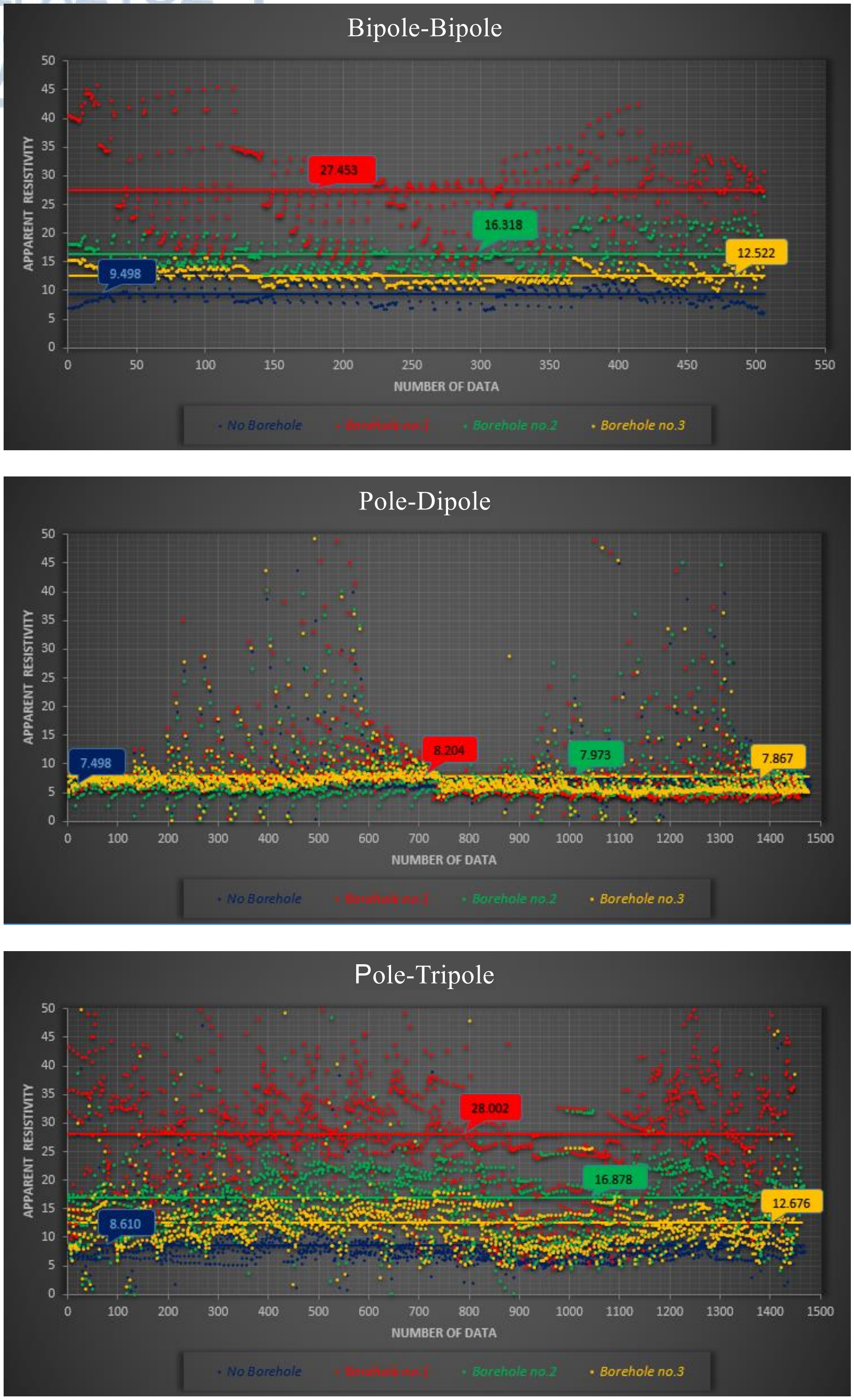

Figure 4.21: Plots of apparent resistivity values and averages (colored lines and frames) apparent resistivity, relative the number of the data points for each array and borehole casing (blue color-no borehole, red color-borehole casing no.1, green color-borehole-casing no.2 and yellow color-borehole-casing no.3).

4.4 Comparison of the average apparent resistivity

Fig.4.22 presents the average apparent resistivity for all the examined electrode arrays, borehole-casings and modelling environments. Different colors correspond to different modelling bodies, with yellow color corresponds to homogeneous medium of water, blue and red colors correspond to conductive and resistive target, respectively. It is a fact that, both bipole-bipole and pole-tripole datasets produce extremely high average apparent resistivities, when the borehole-casing no.1 is used. However, the average apparent resistivity gradually reduces, as the density of the borehole slots increases, approaching the average of the no borehole case. On the contrary, the pole-dipole array presents a normal average apparent resistivity, for all borehole-casings and modelling environments, very close to the value of the no borehole case, presenting though the same gradual reduction trend of the average apparent resistivity, observed in the other arrays, but, to a very limited extent.

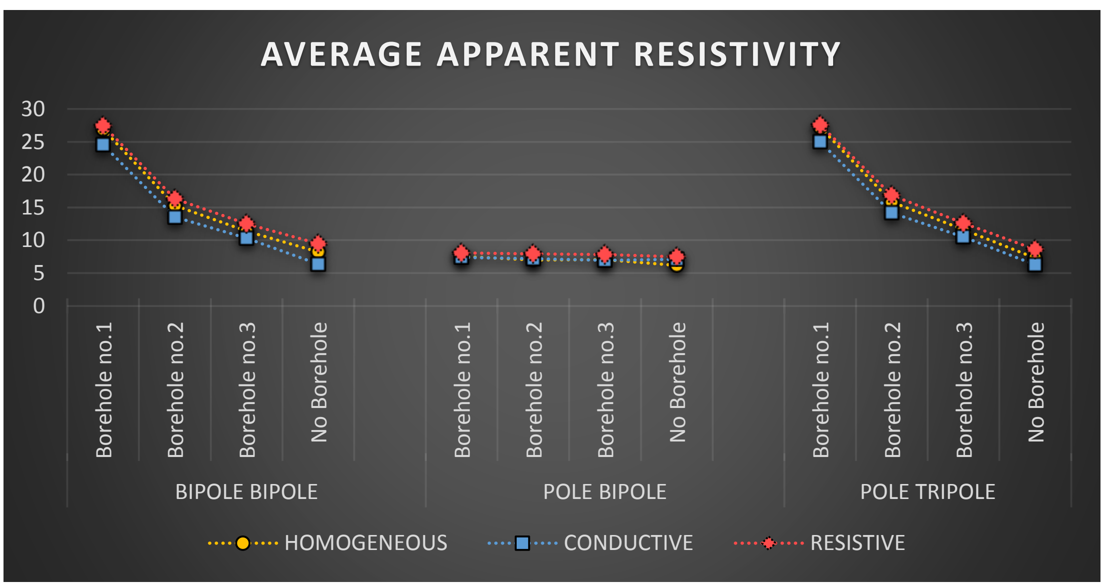

Figure 4.22: Plots of the average apparent resistivity for all arrays and borehole-casing configurations.

In conclusion, all the electrode arrays suffer from the presence of the boreholes, especially, when the borehole-casings have low slot density. It must be pointed out, that the presence of borehole-casings, affects the cross-hole ERT resistivity data, either to a large extent (i.e. bipole-bipole and pole-tripole array), or to a smaller one (i.e. pole-dipole array), depending on the electrode array configuration.

4.5 Conclusions

The experimental cross-hole ERT datasets carried out in a controlled environment and obtained for different electrode array setups and different modelling bodies, using all three tested borehole-casings, of varying slot density, indicated a close relation between cross-hole measurement quality and borehole slot density.

It was observed that, as the number of borehole slots increases, the apparent resistivity values decrease, reaching gradually to value of apparent resistivity for the no borehole case. Essentially, the higher borehole slot density, the better quality of the cross-hole resistivity data. This suggests that, when the borehole-casing has a significant number of slots, the current flows easier outside the boreholes, producing a normal concentration of potential distribution, inside the borehole. On the contrary, when the density of borehole slot density is low, the equipotential contours follow the direction of the borehole and hence, the concentration of potential distribution inside the borehole is exponentially large, leading to highly resistivity values.

In view of the tested electrode arrays, all of them produced datasets that present a significant reduction trend of average apparent resistivity, or, more specifically, a reduction trend of the apparent resistivity values, as the density of borehole slots increases. Clearly, among the tested electrode configurations, the pole-dipole array is the most effective and reliable, since it produced the optimal inversion results, in all cases, resulting simultaneously, in high data quality and limited resistive artefacts. In contrast, bipole-bipole and pole-tripole arrays, produced inversion results of a much lower quality, with major artefacts and generally poor reconstruction of the modelling bodies.

Overall, the cross-hole ERT results of the experimental tests, show that the measurement quality, depends also on the electrode configuration, since the pole-dipole array is much better than bipole-bipole and pole-tripole arrays. This is due to the fact, that none of the injection electrodes of pole-dipole array, is placed into the same borehole with the potential electrodes.

As a final conclusion, the density of borehole slots plays an important role, modulating the current's flow outside the borehole-casings and consequently the data quality. After all, for the best possible effectiveness of the cross-hole ERT measurements, pole-dipole array is clearly the most preferable and reliable electrode array.

CHAPTER 5

Field measurements

In this chapter, the results of the cross-hole ERT field measurement tests, using available monitoring boreholes are presented.

A brief description of the geological/hydrogeological setting of the investigated area is presented. Some general information about the boreholes used for the measurements, such as elevation, length and water level are also provided. Furthermore, the basic details for the general setup and the datasets of the measurements are described.

Several cross-hole ERT measurement tests were carried out, to cross-validate the findings of the experimental tests and to provide information regarding the most efficient ERT measurement configuration between boreholes.

5.1 Introduction

This chapter describes the field ERT measurements, between boreholes, obtained within a framework of a larger geophysical measuring campaign, which was aiming to investigate the subsurface at a particular region where the underground tunnel of the Thessaloniki Metro was under construction.

During the field survey several issues related to the applicability of the cross-hole ERT measurements were raised, mainly due to the relatively long distance between boreholes. To overcome this problem, two methods were applied to improve the ERT resolution, the first had to do with the “enhancement” of the cross-hole ERT data, with surface ERT measurements, while the second one with the application of the borehole-to-surface method, as will be later explained.

The main purpose of this study is to evaluate the applicability of the particular cross-hole measurement arrangement in PVC-cased piezometers and not to focus on the geological/geotechnical interpretation of the geoelectrical images; however, available geological information from core logging, along some boreholes are included to contribute to the assessment of the applied methodology.

5.2 Field methodology

5.2.1 Investigation area

The investigation area of the field survey is located within the city of Thessaloniki, Greece. The geological environment mainly, consists of sedimentary rocks, as sandstone or claystone, and Quaternary deposits of clay, sand, gravel and various mixes of them.

For the realization of the field measurements, six water-level monitoring boreholes (piezometers) were used, as they are presented in Fig.5.1. The piezometers are divided in the old piezometers (white dots), performed during an early stage of the geotechnical investigation project, with an unknown (probably limited to 2-3 slots/m) number of borehole slots, and the new piezometers (orange circles), which, were constructed with a significant higher density of borehole slots (5-7 slots/m). The red and yellow lines in Fig.5.1 represent the field cross-hole ERT tomograms and the borehole to surface tomograms, respectively.

Figure 5.1: Site location of the field measurements.

The piezometers P2, P3 and P4, were also drilled for sampling and inspection of the soil condition and hence, the lithological column was available, as this was derived from the core logging.

Table 3 presents the elevation and the depth of each piezometer, along with the water level elevation (m.a.s.l.).

Borehole ID	Elevation (m)	Depth (m)	Water level (m)
P1	10.15	35	6.30
P2	10.10	28.5	6.50
P3	8.40	28	5.20
P4	8.63	22	5.45
P5	8.95	35	5.70
P6	9.06	35	5.70

Table 3: Information on the piezometers used in this study.

5.2.2 Field measurements equipment

Two specially constructed multi-electrode cables were used, for the realization of the cross-hole measurements, each one with 24 embedded measuring copper electrodes, spaced at a 1 m interval. The 2 cables were inserted within the piezometer in a way that all measuring electrodes were below the water table allowing the galvanic contact between the electrodes and the surrounding. An additional multi-electrode cable was used for the surface measurements, also with 24 measuring electrodes, spaced at a 4 m interval. Moreover, multiplexer boxes were used to connect the cables with the resistivity meter.

Figure 5.2: The equipment used for the field measurements.

Figure 5.3: The borehole and surface electrodes, used for the field measurements.

Overall, the presented field measurements involve 4 locations in which different ERT data collection schemes between boreholes were tested. These locations are marked with letters from A to D, as shown in Table 4, while their position on the map are depicted in Fig. 5.1. Note that, the number of the electrodes at each borehole, for every dataset, depends on the depth of the borehole and the water level, since all of the measuring electrodes must be placed below the water table, for the achievement of the galvanic contact. Also, in the cross-hole ERT tests, the measuring electrodes of the two boreholes, are placed to the same depth level.

Location	Borehole pair	Method
A	P1-P2	cross-hole
B	P3-P4	cross-hole
C	P3-P5	cross-hole + surface
D	P5-P6	borehole-to-surface + surface

Table 4: Boreholes and method(s) applied at every location.

Considering the inversion results, the positions of the electrodes have been corrected by inserting the topography information before the inversion, hence absolute elevations of the electrodes will be shown in the inverted images. Finally, a uniform rainbow logarithmic scale (cold color corresponds to low and hot color to high resistivity value) was used to display the different resistivity distribution of every inversion result.

Figure 5.4: Supplementary photos from the field measurement collection procedure.

5.3 Field inversion results

5.3.1 Location A

The particular field measurement aimed to confirm and cross-validate the experimental findings, and specifically the correlation between the borehole slot density and the cross-hole ERT data quality, as well as the effectiveness of the examined electrode arrays.

Three optimized measurement protocols were produced and used on the basis of the bipole-bipole, pole-dipole and pole-tripole arrays for obtaining the cross-hole ERT datasets for this case study. The measurement geometry for location 1 (cross-hole pair P1-P2) is shown in Table 5.

Case study	Protocol	Distance of boreholes (m)	No. of electrodes	Elevation of top electrode (m)
A	ABB	25.53	44	2.60
	APD		44	
	APT		42	

Table 5: Basic attributes of the measurement protocols, used in location A.

The inversion results collected in location A, are presented in Fig.5.5, together with the geological information from the core logging of borehole 2 (P2). Pole-dipole array inversion results present the lowest RMS error (8%) than all of the other arrays, producing an inversion image of the investigation area exhibiting a good agreement with the lithological stratigraphy of the borehole P2, appearing two resistive bodies corresponding to the silt formation. On the other hand, the other electrode arrays show a strong weakness to successfully reconstruct the subsurface structure, especially around the borehole P2, where very high resistive unrealistic anomalies appeared. Although, the pole-tripole array seems to be more efficient than bipole-bipole array, it presents a higher RMS error (23%) than the bipole-bipole array (11%).

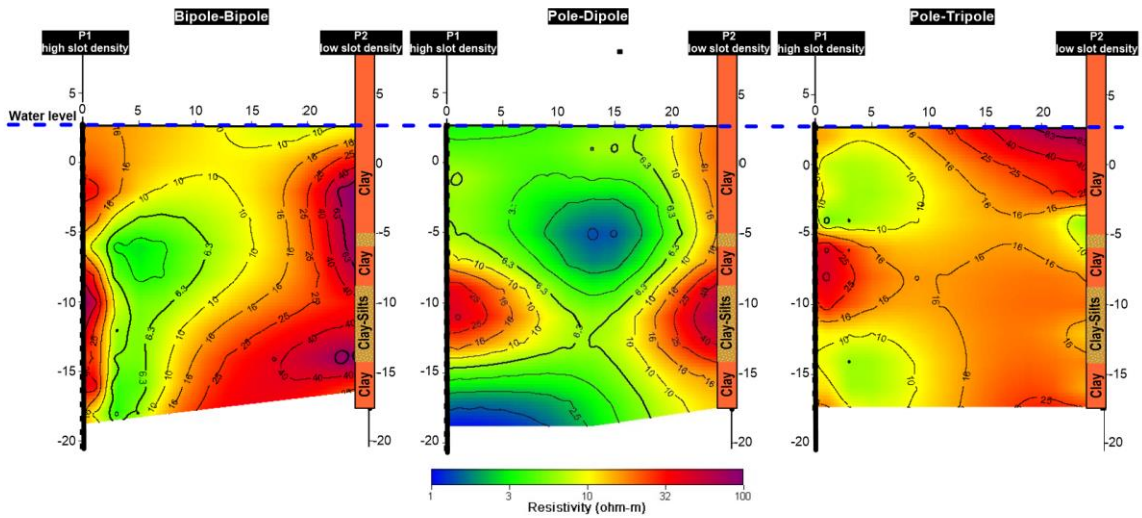

Figure 5.5: 2D cross-hole ERT inversion results for bipole-bipole, pole-dipole and pole-tripole arrays, that were obtained in location A. The P2 borehole log is also depicted.

Table 6, shows the number of the data before and after the inversion process, along with the RMS error for each electrode array. A large number of data (over 40% of the initial data) were excluded, for both bipole-bipole and pole-tripole arrays, indicating poor measurement quality.

Array	Initial no. of data	Final no. of data	RMS error
Bipole-Bipole	464	184	11 %
Pole-Dipole	429	314	8 %
Pole-Tripole	457	272	23 %

Table 6: Basic data attributes of all the arrays used in location A.

For every electrode array, the distribution of the apparent resistivity values and the average apparent resistivity, can be seen in Fig.5.6. As expected, both bipole-bipole and pole-tripole arrays present poor data quality, producing average apparent resistivities, over 1000 Ohm-m, with high dispersion of the data.

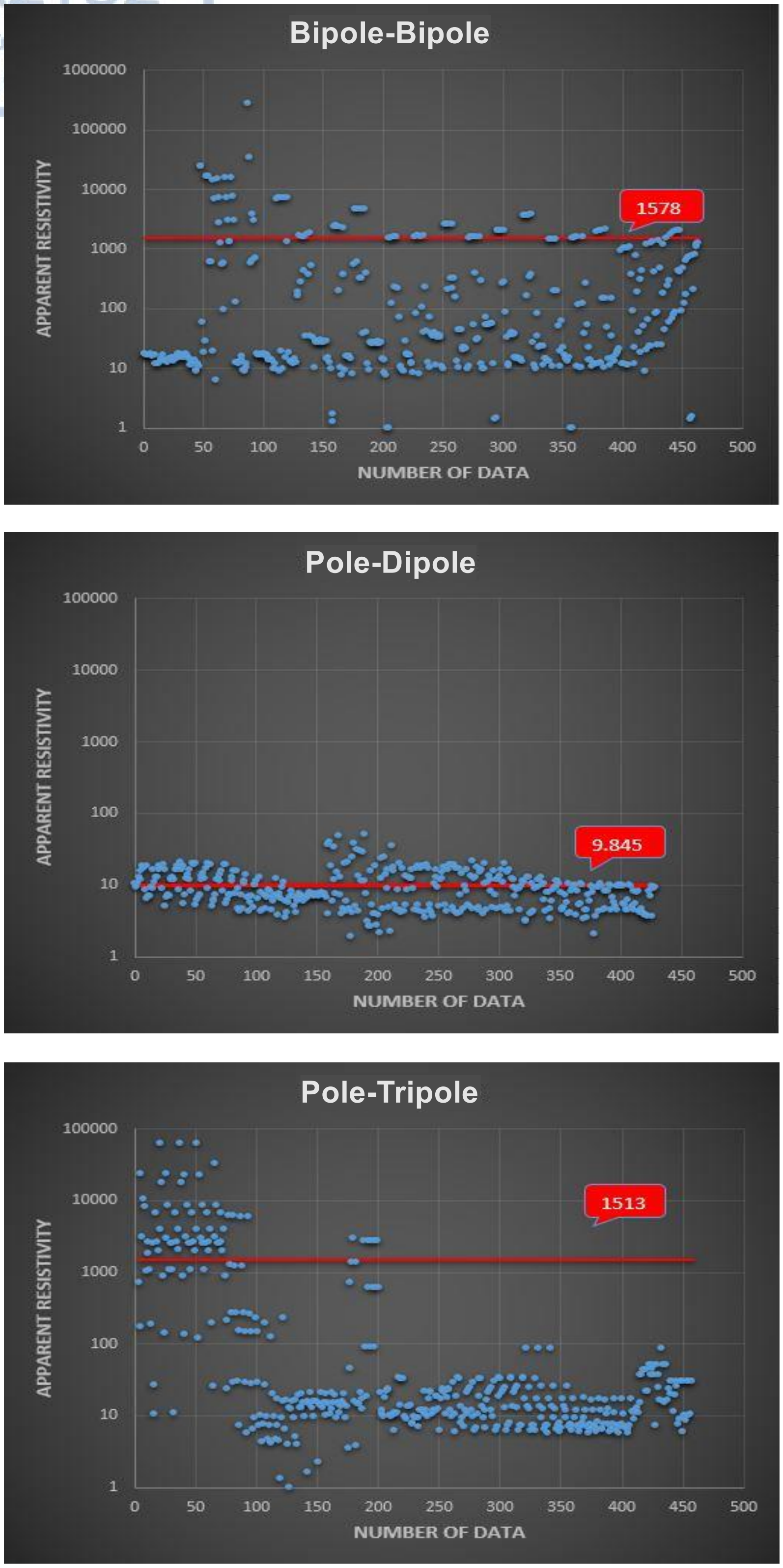

Figure 5.6: Plots of the apparent resistivity values for all examined arrays in area A. In the red frame the average apparent resistivity is presented.

Based on the facts that the potential electrodes of pole-dipole and pole-tripole arrays, respectively, are always placed within the same borehole and the piezometers have different slot density i.e. borehole P1 had a higher slot density than P2, the average apparent resistivity calculated from the potential differences that were collected at each piezometer separately, for these arrays, can easily be computed. This is a purpose of comparison against the effectiveness of pole-dipole and pole-tripole arrays, for the different borehole slot density.

Figure 5.7, shows that the pole-dipole array maintains a constant average apparent resistivity, around 10 Ohm-m, for both boreholes, while the average apparent resistivity of pole-tripole array, from 17 Ohm-m at the borehole P1 (highest slot density), reaches to 3000 Ohm-m at the borehole P2 (very low slot density).

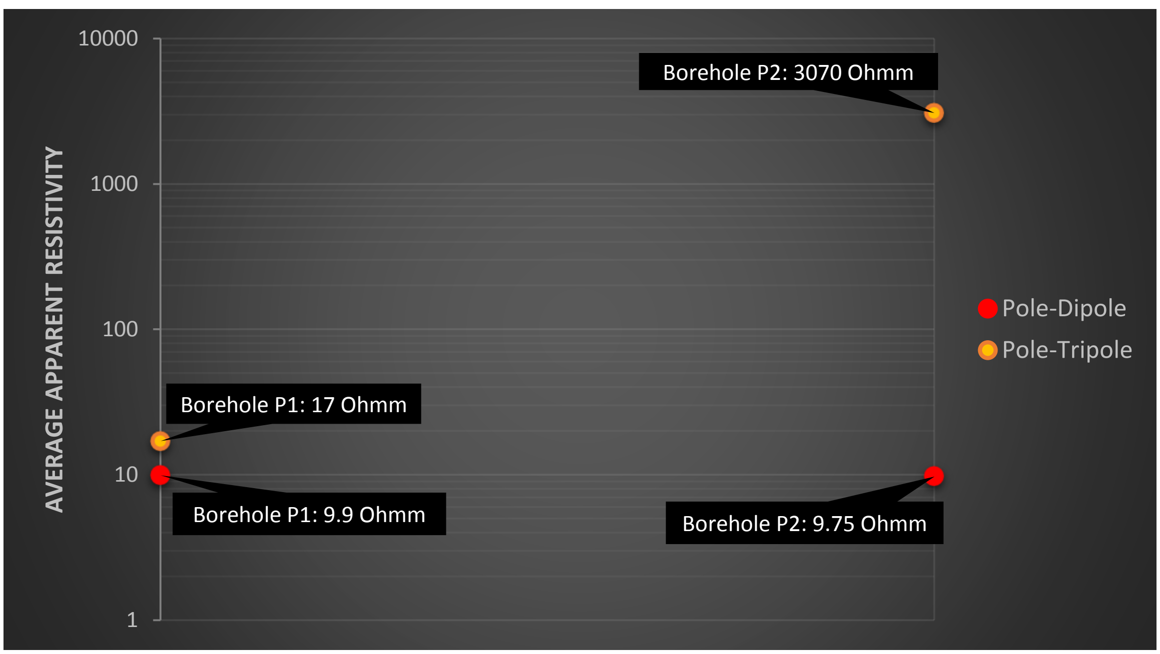

Figure 5.7: Plot of the average apparent resistivity for the pole-dipole and pole-tripole arrays, separately, for each borehole.

This major change of the average apparent resistivity at each piezometer, for the pole-tripole array, is mainly due to the simultaneous presence of the current and potential electrodes within the same borehole. When the borehole has medium-high slot density (P1), the average apparent resistivity, produced by the collected potential differences, is quite realistic, while, when the borehole has a small number of slots (P2), the average apparent resistivity, becomes very high. On the contrary, the pole-dipole array, which has the potential dipole into a different borehole than the current electrodes, does not present a significant variation of the average apparent resistivity for the different slot densities.

Overall, the inversion results for this location, suggest that pole-dipole array can reliably reconstruct the subsurface structure, better than any other array, presenting realistic resistivity values. Furthermore, the above results verified the experimental findings, namely the fact that the data quality and resolving ability depends on the borehole slot density, with denser slots resulting in improved data quality.

5.3.2 Location B

This case study concerns the testing of a different type of measurement for the pole-dipole array, which, generally presented the optimum inversion results in the previous case study, as well as, in the experimental measurements. Moreover, the limited slot density in both P3 and P4 boreholes clearly does not allow the collection of reliable data for the case of the bipole-bipole and pole-tripole arrays and hence, only the pole-dipole array data was collected, for area B.

More specifically, two full dataset measurement protocols were produced on the basis of the pole-dipole array. The only difference between the two protocols is the different placement of the surface remote electrode (5 m and 12.5 m distance from the borehole P3, respectively) for each dataset. After the data acquisition, the two datasets were merged and inverted together.

Protocol	Distance of boreholes (m)	No. of electrodes	Elevation of top electrode (m)	Number of measurements
BPD1	15.80	41	2.95	2818
BPD2				2606

Table 7: Basic attributes for the measurements collected in the location B.

Fig.5.8 presents the combined inverted image of the case study B, between boreholes P3 and P4, together with the geological stratigraphy of the core logging, for both boreholes. Generally, the results produced by the combined inversion of the two data sets of pole-dipole array, provide resistivity distribution with reasonable variations, showing a very good agreement with the geological information.

More specifically, a resistive layer (over 40 Ohmm) is appearing near the surface, corresponding to the clay-silts formation. Below that formation, a quite conductive clay formation, is depicted in the inverted image, which is followed by two more slightly resistive formations (over 25 Ohmm) next to the boreholes, that correspond to the clay-silts formation, as it is shown in the drilling information.

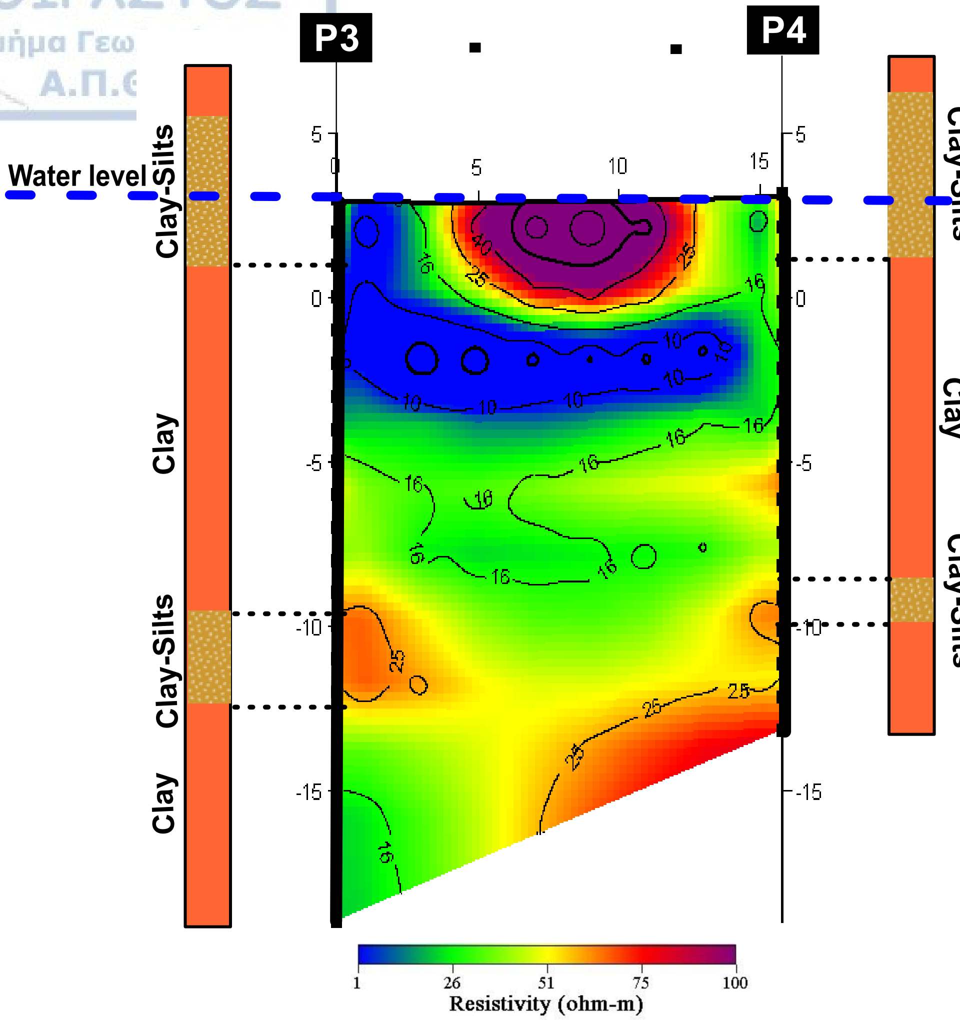

Figure 5.8: 2D inversion results of the pole-dipole array that was used in location B.

5.3.3 Location C

As a result of the good response of the previous inversion scheme of the pole-dipole array, in conjunction with, the long distance between boreholes P3 and P5, of this location, a different variant of the pole-dipole array, was tested in this case study. In addition to the cross-hole dataset, a surface dataset was collected, to enhance the resolving ability at the central part of the area between the boreholes.

Specifically, three full cross-hole ERT protocols and one full surface ERT protocol were produced, for this case study. The cross-hole ERT, datasets were obtained only with the pole-dipole array, with different position of the surface remote electrode, at each dataset, while for the realization of the surface measurements, the conventional multi-gradient array was used. The details of the measurement protocols, for this area are presented in Table 8.

Case study	Data set	Distance of boreholes (m)	No. of electrodes (Borehole)+(Surface)	Elevation of top electrode (m)	No. of measurements
C	DPD1	44	47(B)	3.50	2389
	DPD2			3.50	2083
	DPD3			3.50	2489
	DS	52 m the electrode section	14 (S)	8.50	306

Table 8: Basic attributes of the measurement protocols used for the location C.

The geoelectrical image of the total inverted dataset is illustrated in Fig.5.9, presenting a reasonable resistivity distribution. Overall, a stratified structure is revealed, with a resistive layer up to an average depth of 5m from the surface, corresponding to the clay and silts (but also related to the unsaturated zone) which is followed by a less resistive 5-7m thick layer corresponding to clays. A deeper third layer (10m depth) of similar resistivity and maybe composition to the top one is also depicted in the inverted image.

The results seem to be in a good agreement with the drilling information of borehole P3. The incorporation of the surface ERT measurements into the cross-hole ERT data, provide useful information for the central area that cannot be well covered by the cross-hole ERT, as it is known that the long distance between boreholes, reduces the resolving ability of the cross-hole ERT measurements.

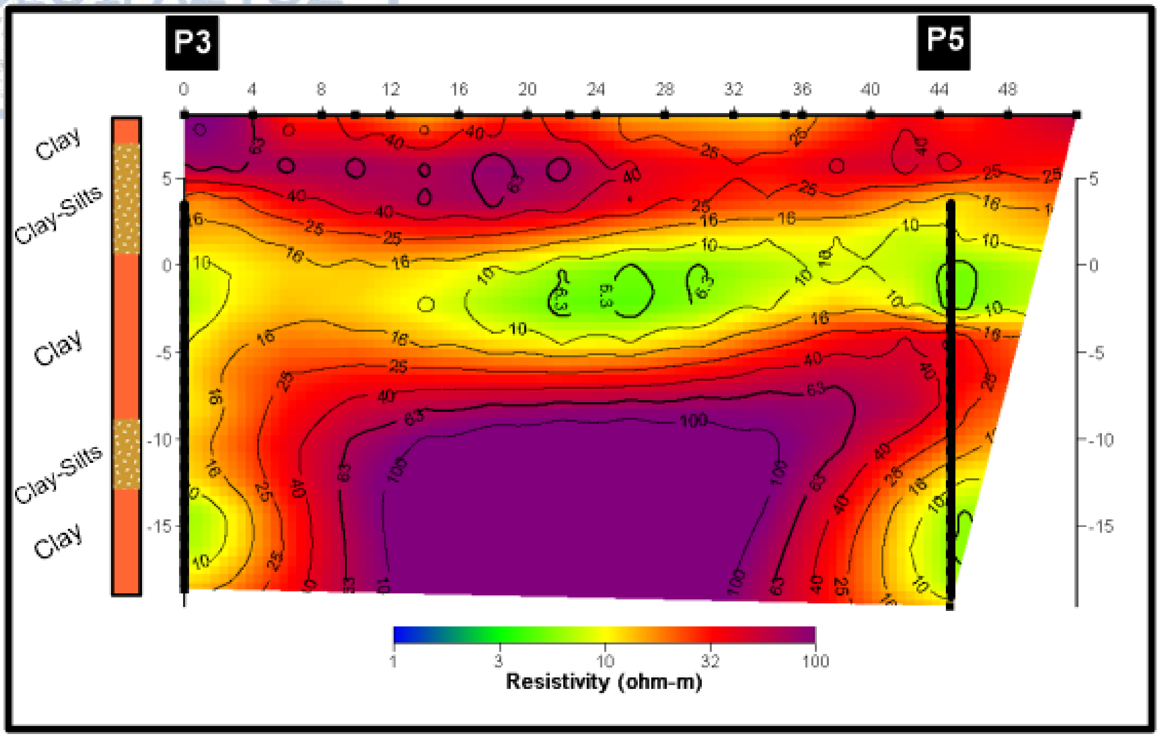

Figure 5.9: 2D inversion results of the combined cross-hole and surface dataset for location C.

5.3.4 Location D

The last case study D, involves the combined inversion of a merged dataset, that was generated as the sum of two borehole-to-surface datasets and one surface dataset. The borehole-to-surface datasets provide information along the boreholes, while the surface dataset, provides valuable information about the top few meters.

As earlier described, the long distance between boreholes, reduces the spatial resolution of the inverted images, especially in the middle section between boreholes. To overcome this limitation, a combination of borehole and surface measurements, the so-called borehole-to-surface, is required to improve the resolution of the resistivity distribution of the investigated area between boreholes.

The sensitivity pattern of a common surface and a borehole-to-surface arrangement, where the borehole is situated in the middle of the section that contains the surface electrodes, is illustrated in Fig.5.10. It has been shown that the combined inversion of the three resulting datasets, of the borehole to surface configuration, can effectively improve the resolution and the quality of the image along the borehole area (Tsourlos et al., 2011).

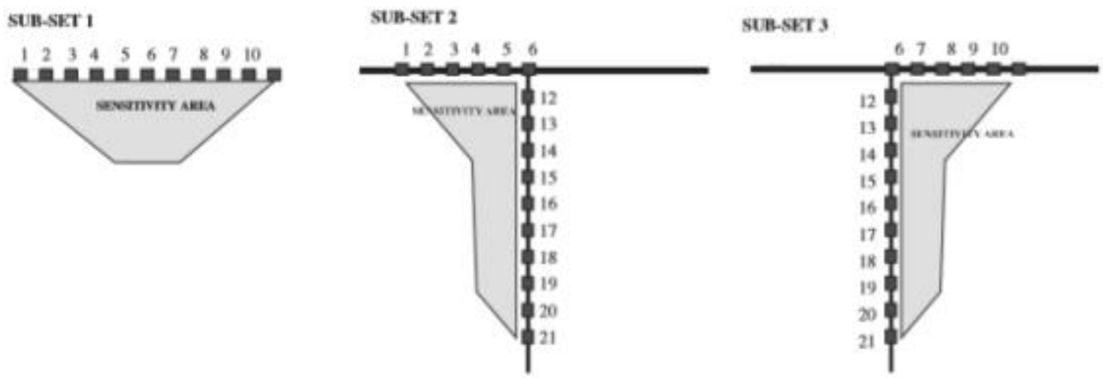

Figure 5.10: Sensitivity pattern of surface (a) and borehole-to-surface (b, c) arrangements (P. Tsourlos et al., 2011).

Based on this inversion scheme, a modified borehole-to-surface arrangement was used in field borehole-to-surface measurement tests between real observation wells (Fig.5.11). According to this configuration, the boreholes are approximately situated at the edges of the section that contains the surface electrodes. This way, three datasets are acquired and merged, namely, one surface and two boreholes to surface datasets, for the combined inversion. The outcome of this borehole-to-surface inversion scheme enhances the imaging resolution of the entire area between boreholes, even if their corresponding distance is quite long.

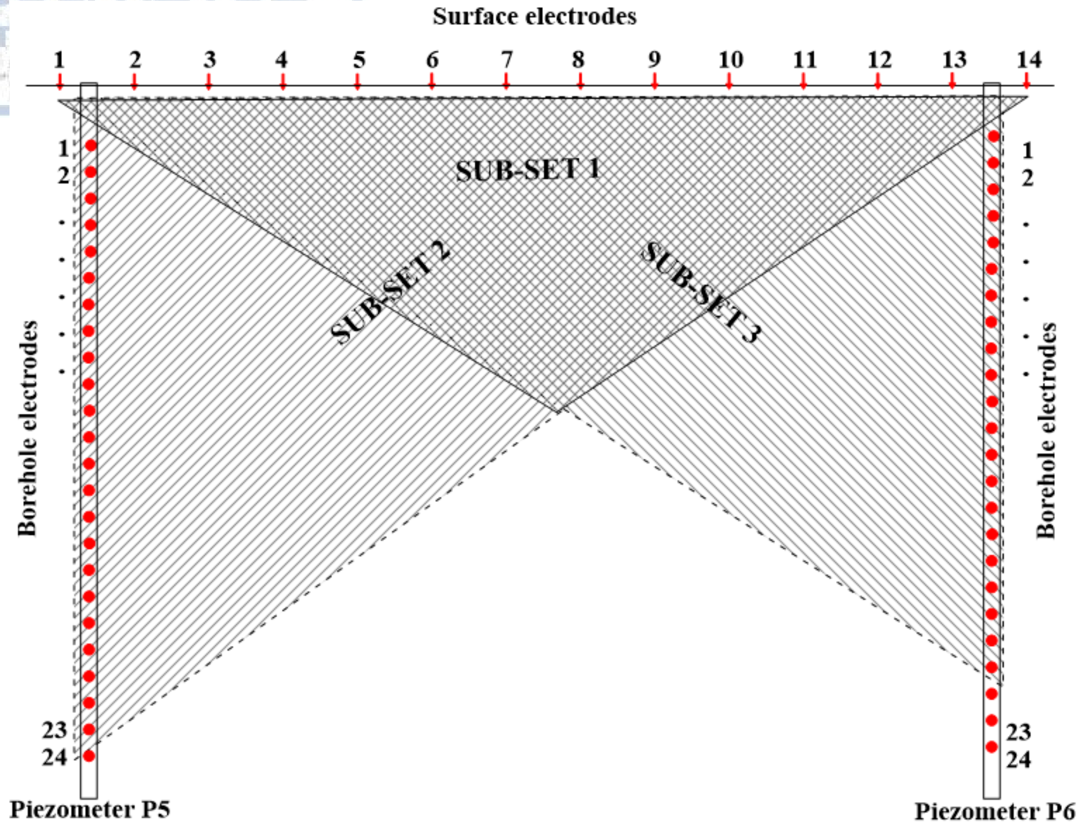

Figure 5.11: Sensitivity pattern of the borehole-to-surface arrangement for each sub-set.

Fig.5.12 presents the actual measuring scheme, applied between boreholes P5 and P6. The surface section contains 14 equally spaced electrodes, while the measurement setup for each borehole involves 24 equally spaced electrodes. The borehole-to-surface datasets were obtained with a dipole-dipole array with the current dipole being always on the surface and potential dipole always into the borehole. For the acquisition of the surface measurements, the conventional multi-gradient array was used. Note that all datasets share the same surface electrodes.

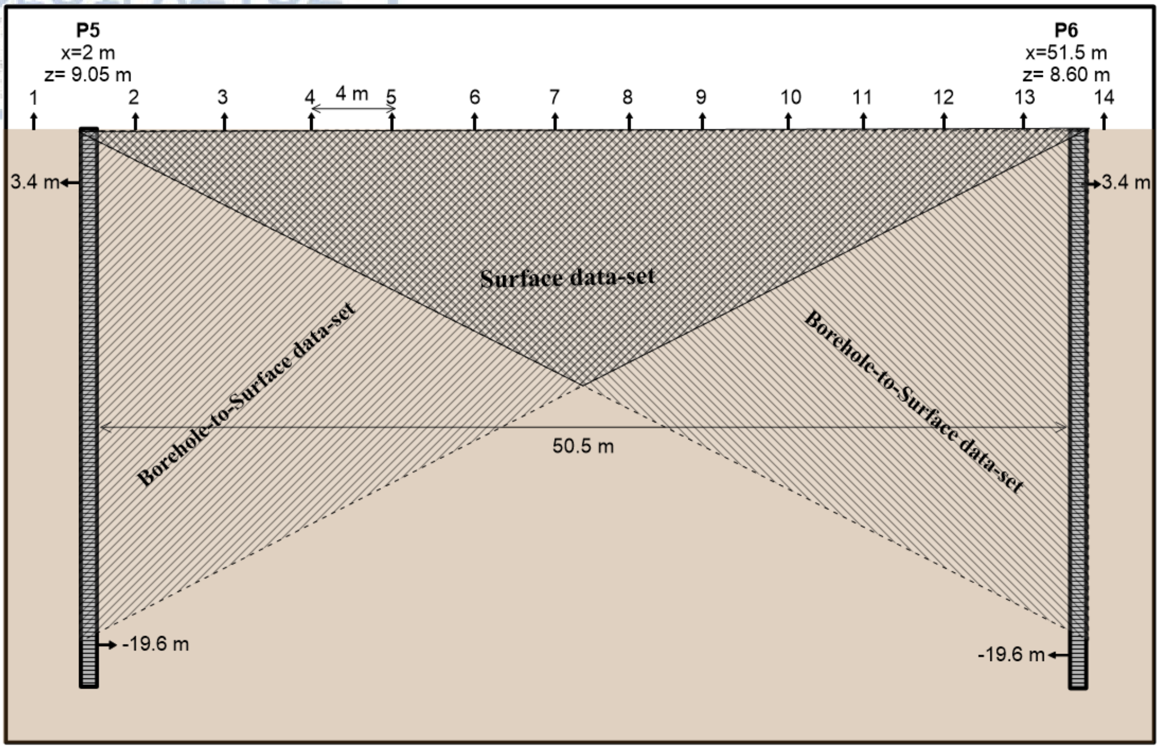

Figure 5.12: Geometry of the borehole-to-surface arrangement involving a surface dataset, applied in location D.

Fig.5.13 presents the inversion results of all the datasets, separately. It is obvious that each dataset cannot individually provide a comprehensive image for the entire area. The borehole-to-surface datasets produce reliable results only for the area around and near the boreholes, while the surface dataset provide information mainly for the central area.

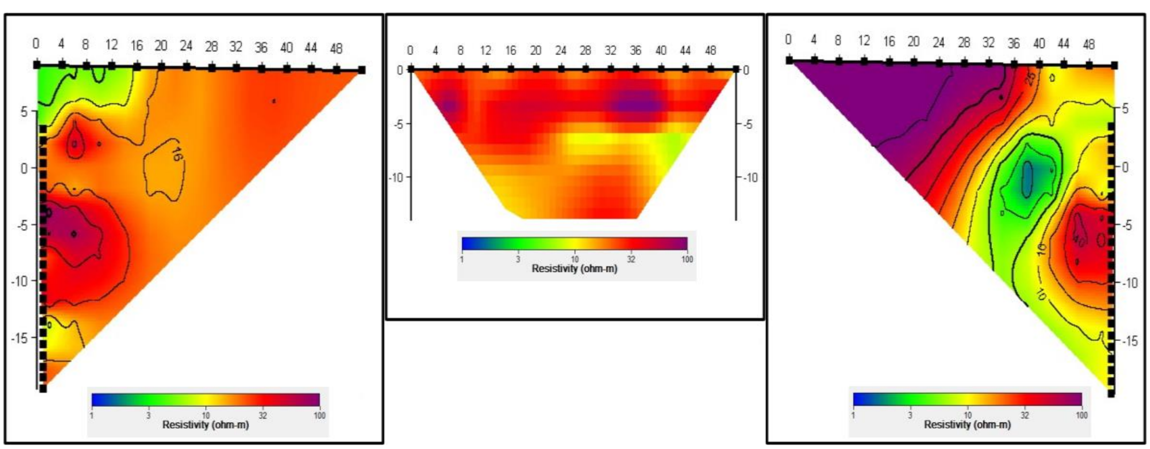

Figure 5.13: Separate inversion results of the borehole-to-surface (left & right) and surface (middle) datasets.

The merging of the three datasets is expected to provide a more complete sensitivity coverage to the entire investigation area. The inversion result of the merged dataset is illustrated in Fig.5.14 and although no drilling information is available the geological model of the stratified earth is in very good agreement with the geological model of the area, as it was already shown in the previous case that involves the borehole P5.

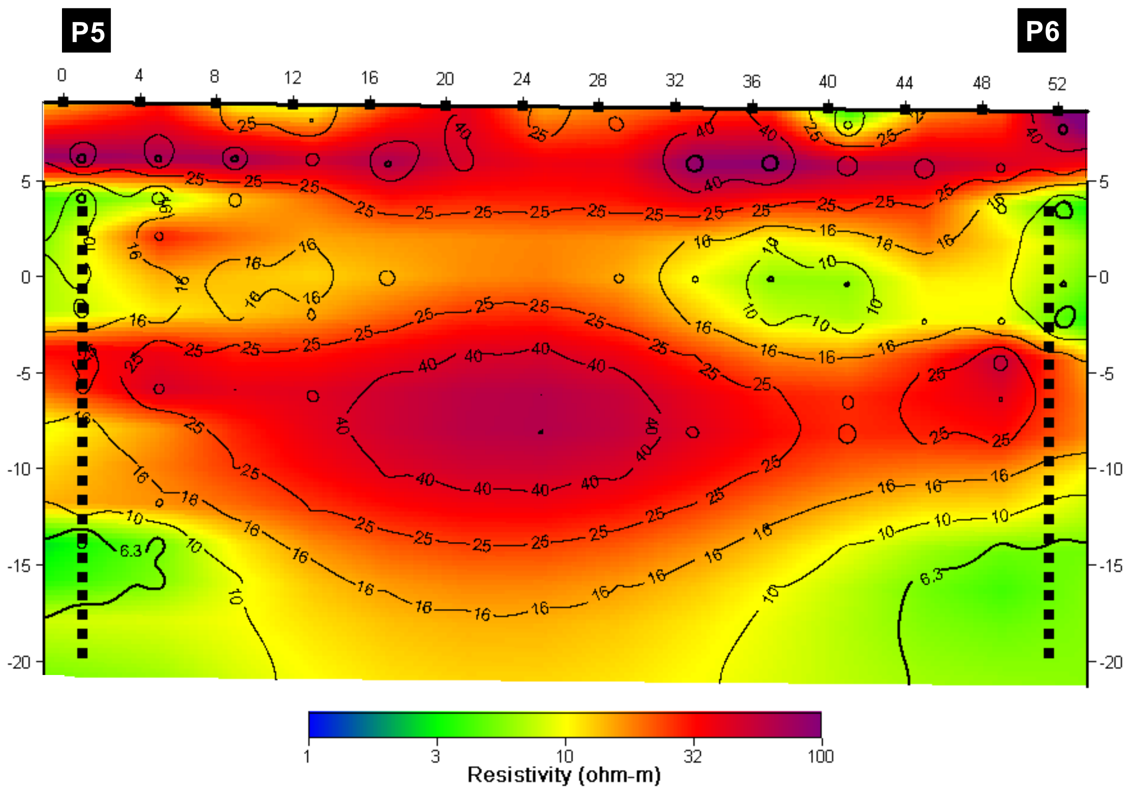

Figure 5.14: Inversion results of the borehole-to-surface arrangement at location D.

5.4 Field data: Concluding remarks

The results of the first case study, using all the electrode arrays, confirmed the experimental findings that the boreholes with a smaller number of borehole slots, affect the data quality more than the denser slots boreholes, suggesting that the pole-dipole array, where the current pole is not in the same borehole with the potential electrodes, is the most preferable array.

This capability of pole-dipole array to remain unaffected by the presence of boreholes, even if the boreholes have a small number of borehole slots, was also confirmed in the case study B, where both boreholes had a limited number of borehole slots. Also, the combined inversion of two data sets, obtained with the pole-dipole array, reconstructed effectively and reliably the subsurface structure.

The problem of the long distance between boreholes, as in the case study C, was addressed with the combined inversion of cross-hole and surface datasets, obtained with the pole-dipole array and the conventional multi-gradient array, respectively. Although, the pole-dipole array itself presented very good results, mainly along the boreholes, the incorporation of the surface measurements, improved the image quality all over the investigation area.

Finally, in area D, the inversion scheme using both borehole-to-surface and surface datasets, produced very good inversion results, despite the long distance between the boreholes. Therefore, the employed setting can be considered as a good approach in cases where the distance between boreholes is too large to be imaged only with cross-hole arrangements. This is of course feasible only when surface measurement can be technically realized.

CHAPTER 6

Conclusions

The structure of the present study is divided into two parts. The first part concerns the experimental measurement tests, where various cross-hole ERT datasets were obtained for different electrode arrays and different modelling bodies, using various test borehole-casings, in order to examine the influence of the different borehole slot density. Several important conclusions were obtained from the inversion results of the measurement tests and are summarized below:

- The cross-hole ERT measurement applicability and the data quality depend on the borehole slot density, with denser slots resulting in improved data quality.
- The existence of both current and potential electrodes within the same borehole, combined with the limited slot density, results affects in a negative manner the measured potential differences and subsequently the ability to obtain the “real” resistivity of the investigation area.
- As a result, the measurement data that were acquired with bipole-bipole or pole-tripole array (i.e. current electrode in the same borehole together with at least a potential electrode), produce high apparent resistivity values, presenting inverted images with significant resistive artefacts.

- Among the tested electrode configurations, the pole-dipole array is clearly the most effective and reliable array, producing high data quality, even if the boreholes have a limited number of borehole slots.

The second part of this work involved cross-hole ERT measurement tests and the application of alternative measurement setups between real observation wells. Several conclusions were drawn regarding the improvement of the data quality and the resolving ability of the surveyed area between boreholes.:

- The field cross-hole ERT measurement tests confirmed the experimental findings related to the cross-hole measurement applicability into slotted boreholes. Datasets that were obtained with bipole-bipole and pole-tripole arrays, produced unrealistic apparent resistivity values, and hence low resolving ability.
- The pole-dipole array, that presented the best inversion results of all the other arrays, was used to collect datasets of partially different electrode setups (different position of the surface remote electrode), suggesting a new electrode configuration scheme for obtaining measurements between boreholes.
- A long distance between boreholes can be handled either with the use of the pole-dipole array, incorporating surface measurements, or with the simultaneous measurement between borehole and surface (borehole-to-surface configuration), involving also surface measurements.

References

Athanasiou E. (2009). Development of algorithms producing optimum strategies for measuring and inverting electrical resistivity tomography (ERT) data. PhD thesis, AUTH.

Auken E, Pellerin L, Christensen NB, Sorensen K (2006). A survey of current trends in near-surface electrical and electromagnetic methods. Geophysics, 71(5): 249-260.

Barker, R. D. (1981). The offset system of electrical resistivity sounding and its use with a multicore cable. Geophysical prospecting, 29(1), 128-143.

Cho, I. K., Lee, K. S., Kim, Y. J., and Kim, K. S. (2016, September). Reduction of 3D Borehole Effects in the Inversion of 2.5 D crosshole ERT Data. In Near Surface Geoscience 2016-22nd European Meeting of Environmental and Engineering Geophysics.

Constable, S. Parker. R., and Constable C. (1987). Occam's inversion: A practical algorithm for generating smooth models from electromagnetic sounding data. Geophysics, 52, 289-300.

Dahlin, T., Zhou, B. (2004). A numerical comparison of 2D resistivity imaging with 10 electrode arrays. Geophysical prospecting, 52(5), 379-398.

Daily W. and Owen E. (1991). Cross-borehole resistivity tomography. Geophysics 56(8), 1228–1235

Dey, A., and Morrison, H. F. (1979). Resistivity modelling for arbitrarily shaped two-dimensional structures. Geophysical Prospecting, 27(1), 106-136.

Doetsch, J. A., Coscia, I., Greenhalgh, S., Linde, N., Green, A., and Günther, T. (2010). The borehole-fluid effect in electrical resistivity imaging. Geophysics, 75(4), F107-F114.

Farquharson, C. G., and Oldenburg, D. W. (1998). Non-linear inversion using general measures of data misfit and model structure. Geophysical Journal International, 134(1), 213-227.

Goes, B. J. M., and Meekes, J. A. C. (2004). An effective electrode configuration for the detection of DNAPLs with electrical resistivity tomography. Journal of Environmental and Engineering Geophysics, 9(3), 127-141.

Griffiths DH, Turnbull J, Olayinka AI (1990). Two-dimensional resistivity mapping with a complex controlled array. First Break, 8: 121-29.

Inman Jr, J. R., Ryu, J., and Ward, S. H. (1973). Resistivity inversion. Geophysics, 38(6), 1088-1108.

Jackson, D. D. (1972). Interpretation of inaccurate, insufficient and inconsistent data. Geophysical Journal of the Royal Astronomical Society, 28(2), 97-109.

Jepsen, A. F. (1969). Numerical modelling in resistivity prospecting. University of California, Department of Materials Science and Engineering, Engineering Geoscience.

Kim, J.H., (2013). DC2DPro – User's Manual, KIGAM, KOREA.

Lee, T. (1975). An integral equation and its solution for some two-and three-dimensional problems in resistivity and induced polarization. Geophysical Journal of the Royal Astronomical Society, 42(1), 81-95.

Leontarakis, K., and Apostolopoulos, G. V. (2012). Laboratory study of the cross-hole resistivity tomography: the model stacking (MOST) technique. Journal of Applied Geophysics, 80, 67-82.

Leontarakis, K., and Apostolopoulos, G. V. (2013). Model Stacking (MOST) technique applied in cross-hole ERT field data for the detection of Thessaloniki ancient walls' depth. Journal of Applied Geophysics, 93, 101-113.

Loke, M.H, Acworth, I., Dahlin, T. (2003). A comparison of smooth and blocky inversion methods in 2D electrical imaging surveys. Exploration Geophysics, 34(3), 182-187.

Loke, M. H., and Barker, R. D. (1995). Least-squares deconvolution of apparent resistivity pseudosections. Geophysics, 60(6), 1682-1690.

Loke M.H., (2016). RES2DINV – User's Manual, Geotomosoft Solutions, Malaysia.

Madden, T. R. (1967). Calculations of induced polarization anomalies for arbitrary two-dimensional resistivity structure Proc. Symp. on IP. University of California, Berkeley.

Menke, W., 1989, Geophysical Data Analysis: Discrete Inverse Theory (Revised edition). Academic Press Inc. IBSN 0124909213

Mufti, I. R. (1976). Finite-difference resistivity modeling for arbitrarily shaped two-dimensional structures. Geophysics, 41(1), 62-78.

Narayan, S., Dusseault, M.B., Nobes, D.C. (1994). Inversion techniques applied to resistivity inverse problems. Inverse Problems, 669-686.

Nimmer, R. E., Osiensky, J. L., Binley, A. M., and Williams, B. C. (2008). Three-dimensional effects causing artifacts in two-dimensional, cross-borehole, electrical imaging. Journal of Hydrology, 359(1-2), 59-70.

Okpoli, C. C. (2013). Sensitivity and resolution capacity of electrode configurations. International Journal of Geophysics, 2013.

Osiensky, J. L., Nimmer, R., and Binley, A. M. (2004). Borehole cylindrical noise during hole–surface and hole–hole resistivity measurements. Journal of Hydrology, 289(1-4), 78-94.

Pelton, W. H., Rijo, L., and Swift Jr, C. M. (1978). Inversion of two-dimensional resistivity and induced-polarization data. Geophysics, 43(4), 788-803.

Ramirez, A. L., Daily, W. D., and Newmark, R. L. (1995). Electrical resistance tomography for steam injection monitoring and process control. Journal of Environmental and Engineering Geophysics, 1(A), 39-51.

Smith, N. C., and Vozoff, K. (1984). Two-dimensional DC resistivity inversion for dipole-dipole data. IEEE Transactions on Geoscience and Remote Sensing, (1), 21-28.

Shima, H. (1992). 2-D and 3-D resistivity image reconstruction using crosshole data. Geophysics, 57(10), 1270-1281.

Simyrdanis K., Tsourlos, P., Soupios, P., Tsokas, G. (2013). Simulation of ERT surface-to-tunnel measurements. Bulletin of the Geological Society of Greece, 47, 1251-1259.

Tarantola, A. (1987). Inverse Problem Theory: Methods for Data Fitting and Model Parameter Estimation. Paris, France: Elsevier Science Publishing Company INC.

Telford, W. M., and Geldard, L. P. Sheri¡, RE and Keys, DA, 1976. Applied Geophysics.

Telford, W.M., Geldard, L.P., Sheriff, R.E. (1991). Applied Geophysics, 2nd edition.

Tikhonov, A.N. (1963). Solution of incorrectly formulated problems and the regularization method. Soviet Mathematics. 4. 1035-1038.

Tong, L. T., and Yang, C. H. (1990). Incorporation of topography into two-dimensional resistivity inversion. Geophysics, 55(3), 354-361.

Tsourlos, P. (1995). Modelling, Interpretation and Inversion of Multielectrode Resistivity Survey Data. University of York.

Tsourlos, P., Ogilvy, R., Papazachos, C., and Meldrum, P. (2011). Measurement and inversion schemes for single borehole-to-surface electrical resistivity tomography surveys. Journal of Geophysics and Engineering, 8(4), 487.

Ward, S. H. (1990). Geotechnical and environmental geophysics. Society of Exploration Geophysicists, 352.

Wiggins, R. A. (1972). The general linear inverse problem: Implication of surface waves and free oscillations for earth structure. Reviews of Geophysics, 10(1), 251-285.

Wilkinson, P.B., Meldrum, P.I., Kuras, O., Chambers, J.E., Holyoake, S.J., Ogilvy, R.D., (2010). High-resolution Electrical Resistivity Tomography monitoring of a tracer test in a confined aquifer. Journal of Applied Geophysics, 268-276.

Zhou, B., and Greenhalgh, S. A. (2000). Cross-hole resistivity tomography using different electrode configurations. Geophysical prospecting, 48(5), 887-912.

Zhou, B., and Greenhalgh, S. A. (1997). A synthetic study on crosshole resistivity imaging using different electrode arrays. Exploration Geophysics, 28(1/2), 1-5.